New Jersey Institute of Technology

Digital Commons @ NJIT

Summer 8-31-2003

Deposition and characterization of laser-ablated silicon

Wenwen Luo
New Jersey Institute of Technology

Follow this and additional works at: https://digitalcommons.njit.edu/theses

Part of the Electrical and Electronics Commons

Recommended Citation

ABSTRACT

DEPOSITION AND CHARACTERIZATION OF LASER-ABLATED SILICON

by
Wenwen Luo

Laser ablation is a powerful thin film deposition and material processing technology. In the Nonlinear Nanostructure Lab at NJIT, silicon films deposited by laser ablation have been studied for the potential applications in nonlinear optoelectronic devices. The previous studies have suggested that the deposited silicon has a hexagonal symmetry, being a polymorph of silicon that previously has been obtained only at very high pressure. This thesis is part of the continuous study and characterization of this new structure. The objective of the research was to gain better understanding of the hexagonal silicon properties as well as the mechanism that lead to hexagonal silicon formation.

The laser ablation of the silicon nanostructure was done with nanosecond pulsed 532 nm ultraviolet laser in vacuum chamber. Different substrates of quartz and aluminum-coated quartz were used. The ablated silicon film consists of a smooth featureless matrix embedded with crystalline droplets. The micro-Raman spectra measurements revealed that the droplets have a hexagonal symmetry. The topographical properties were studied with combination of scanning electron microscope and atomic force microscope. And its mechanical properties were investigated by nanoidentation using scanning force microscope. The effects of annealing were studied under different temperature and annealing ambient. The annealing conditions that convert the hexagonal silicon to cubic diamond silicon were established. Based on the study, a tentative mechanism of forming the hexagonal silicon was proposed.

DEPOSITION AND CHARACTERIZATION OF LASER-ABLATED SILICON

by

Wenwen Luo

A Thesis
Submitted to the Faculty of
New Jersey Institute of Technology
In Partial Fulfillment of the Requirements for the Degree of
Master of Science in Electrical Engineering

Department of Electrical and Computer Engineering

August 2003

Blank Page

APPROVAL PAGE

DEPOSITION AND CHARACTERIZATION OF LASER-ABLATED SILICON

Wenwen Luo

Dr. Márek Sosnowski, Thesis Advisor   Date
Professor, Department of Electrical and Computer Engineering, NJIT

Dr. Haim Grebel, Thesis Co-Advisor   Date
Professor, Department of Electrical and Computer Engineering, NJIT

Dr. Zafar Iqbal , Committee Member   Date
Research Professor, Department of Chemistry and Environmental Science, NJIT

BIOGRAPHICAL SKETCH

Author: Wenwen Luo

Degree: Master of Science

Date: August, 2003

Undergraduate and Graduate Education:

- Master of Science in Electrical Engineering,
  New Jersey Institute of Technology, Newark, NJ, 2003

- Bachelor of Science in Electrical Engineering,
  Fudan University, Shanghai, P. R. China, 2000

Major: Electrical Engineering

This dissertation is dedicated

to my family, especially to my beloved mother

ACKNOWLEDGMENT

I wish to express my deepest appreciation to my advisors, Professor Marek Sosnowski and Professor Haim Grebel, for their great guidance throughout the whole research. Without their support, I could never complete this research topic.

Special thanks to Dr. Zafar Iqbal for serving on the thesis committee and letting me to use the instruments in his lab.

I would like to thank Dr. Leszek Gladczuk, Dr. Yan Zhang, Dr. Xueyan Zhang, Dr. Aidong Lan, and Ms. Jing Chen for the help during the experiments.

Finally, I would like to thank my parents, my sister and my husband for their continuous support and encouragement.

TABLE OF CONTENTS

TABLE OF CONTENTS
(Continued)

LIST OF TABLES

x

CHAPTER 1

INTRODUCTION

1.1 Research Motivation and Scope

Silicon (Si) has been the foundation material for the electronic and computer technology. It also plays significant roles in other fields such as the miniaturized mechanical and optical devices. The silicon crystal used in the electronic industry has a cubic diamond structure, which is the common phase for the silicon crystal under atmospheric pressure up to the melting temperature. The cubic diamond structure belongs to the space group of Fd3m and is labeled as Si-I. About three decades ago, the first high-pressure polymorphs of silicon were found in diamond anvil pressure cell experiments [1]. Since then, not less than 12 different types of silicon polymorphs have been observed in the high pressure experiments or under contact loading conditions [1, 2]. For example, at pressure of 10 to 13 GPa, silicon undergoes a semiconductor-to-metal phase transition from the cubic diamond phase (Si-I) to a β-tin phase (space group I4$_1$/amd) [2]. The β-tin phase is labeled as Si-II. This transformation is non-reversible. Instead, the β-tin phase (Si-II) will transform to other silicon polymorphs depending on the different rate of pressure releasing, If the pressure is slowly released, the Si-II structure will transform to a rhombohedral polymorph around 10 – 12 GPa, which is also known as r8 phase or Si-XII (space group $R\bar{3}$). The r8 phase can be reversibly transformed to the body-centered cubic bc8 phase (Si-III, space group $Ia\bar{3}$) at 2 GPa. When the pressure is rapidly released, two tetragonal polymorphs with unknown structures have been observed [1]. Another polymorph, Si-IV, which has a hexagonal wurzite structure (space group P6$_3$/mmc),

has been formed by heat treatment of Si-III at 200 – 600 °C or from plastic deformation of Si-I at high temperatures of 350 – 700 °C and confining pressure [2].

There is scientific and engineering significance to understanding of various properties of the silicon polymorphs. The knowledge of the behavior of the silicon under hydrostatic pressure or contact loading such as the indenting, scratching, or machining is vital for the reliability of the silicon based mechanical devices. The study of the phase transformation and amorphization has been the main topic of the emerging research area of high-pressure surface science of silicon [2]. However, there have not been enough experimental data due to the instability of the silicon polymorphs at ambient pressure.

In the Nonlinear Nanostructures Laboratory at NJIT, one type of the silicon polymorphs, i.e. the hexagonal-wurtzite silicon phase has been obtained by laser ablation of the common phase of silicon [3, 4]. An interesting feature of the laser-ablated hexagonal silicon is its enhanced nonlinear optical behavior, which might lead to novel optoelectronic applications [4]. The laser-ablated polymorph is stable at room pressure, which facilitates the investigation of its mechanical and electrical properties. The availability of the stable hexagonal silicon phase not only allow us to investigate the properties of the hexagonal silicon itself, but also enables us to study the phase transition between the hexagonal silicon and other phases of silicon.

This thesis is a part of the continuing experimental investigation of this uncommon silicon phase of NJIT. In this research, the hexagonal-wurtzite silicon polymorphs were prepared from <100> cubic diamond single-crystal silicon by 248 nm KrF laser ablation. The hexagonal structure was identified by micro-Raman spectroscopy. The mechanical and electrical properties of the hexagonal silicon were studied. The phase

transformation behavior of the hexagonal silicon was investigated under different annealing temperature and annealing ambient. The main objective of the research is to achieve a better understanding of the properties of laser-ablated hexagonal silicon.

1.2 Organization of the Thesis

Chapter 2 introduces the thin film deposition method of laser ablation and summarizes the prior work on the laser ablated hexagonal silicon at NJIT's Nonlinear Nanostructures Lab.

Chapter 3 describes the experimental methods used in the research. It introduces various characterization methods such as Raman spectroscopy, scanning electron microscope, atomic force microscope (AFM), nanoindentation and various mechanical and electrical characterizations.

Chapter 4 presents the experimental results and discussions of the results. The results are compared with the prior investigations.

Finally, chapter 5 concludes the thesis and proposes topics of future work.

CHAPTER 2

LASER ABLATION

2.1 Principles

Laser ablation, also known as pulsed laser deposition (PLD), is a powerful mean to deposit a wide range of materials. The process involves a series of interactions between the pulsed laser beam and the target surface. It is not just simple thermal evaporation of the target material. Instead, the photo-excitation of electrons plays a dominant role in the process. Many other effects can also result from the laser-target interaction such as the laser-induced desorption or ionization. Laser ablation should only be defined when 1) the removal of the material is more than one monolayer per laser pulse; 2) atom, ion or cluster yields are linear function of the electronic excitation density; 3) a fluence threshold exists below which only particulate emission occurs without surface destruction [5].

The sequence of steps of laser-target interaction in the laser ablation is illustrated in Fig.2.1. It starts with the interaction of the photons with a crystal surface that generates electron-hole pairs. This excitation process of the electrons includes electronic transitions from valence band states and from the occupied surface and defect states to the states of conduction band. The relaxation of the electron excitation by the electron-lattice interaction results in a metastable state of the surface layer. The electron-lattice interaction includes several mechanisms such as the scattering of free electrons by phonons, local lattice rearrangement and defect formation or surface decomposition. A secondary electronic process that accompanies or follows the electron-lattice interaction

4

Target Crystal

photo-excitation

Electron-Hole Pairs

self-trapping or electron-hole capture

Relaxed Excited States

non-radiative defect reaction

Metastable States

photo-excitation

Vacancy and Emitted Atoms

photo-excitation

Vacancy Clusters and Emitted Atoms

*Ejection of atoms and
molecules from the surface*

Laser-ablated thin film
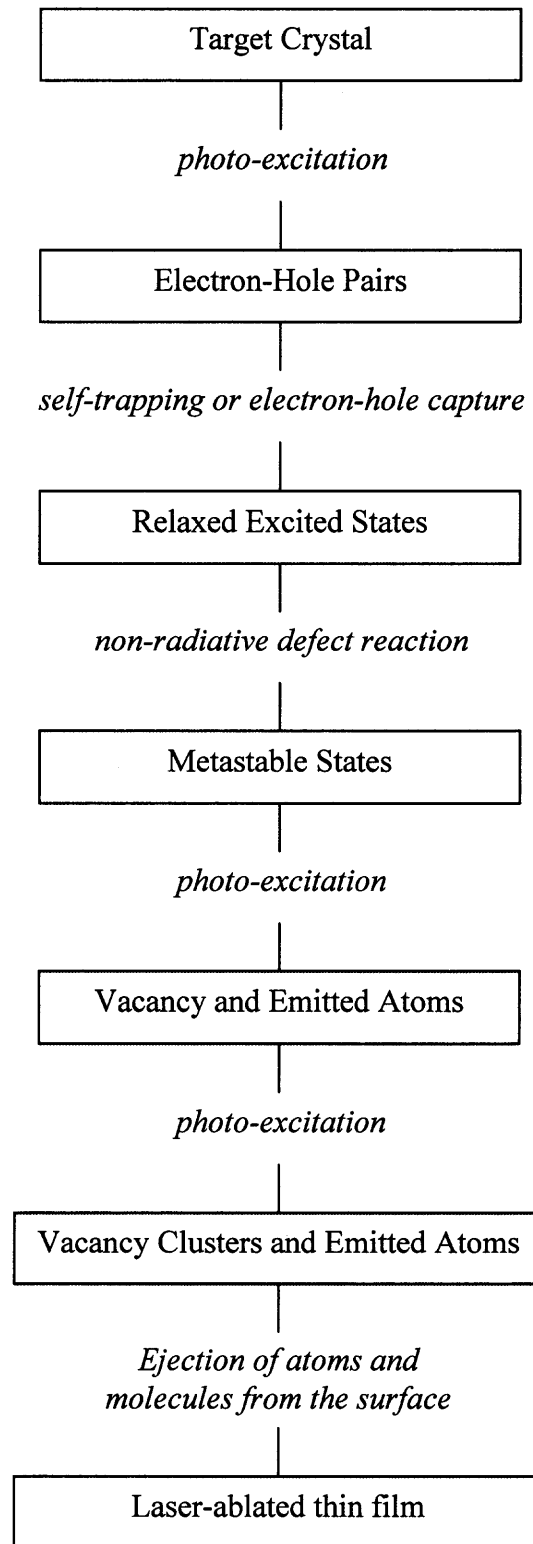
Fig.2.1: The electronic process steps in the laser ablation [5]

causes the defects and defect clusters to grow in number and evolve into the sub-surface bulk. When the photon excitation is strong enough to cause direct nuclear motion of ejection of atoms, ions and molecules from the target surface, the laser ablation process starts.

The real ablation process is more complicated and many aspects of the underlying chemistry and physics are still not fully known. One way to categorize the process is by comparison the photon energy and the band gap of the target material [5]. For situation of $hv < Eg$, only a multi-photon band-to-band transition occurs with very small effective transition cross-section. When $hv > Eg$, the excess laser energy is transformed into phonons and heat the target up very quickly. In our experiments, a KrF laser with $hv = 5$ eV is used to ablate silicon target of band gap $Eg = 1.1$ eV. A strong heating and melting of the target material is expected, which might be described as "thermal ablation".

2.2 Thin Film Growth Mechanism

A thin film starts to grow as soon as the ablation plume hits the substrate. The growth mechanism is influenced by several factors including the target material, the ablation ambient, as well as the substrate and its temperature. In this research, the substrate is kept at room temperature, which is much lower than the nucleation temperature. The film deposited under such condition is expected to be amorphous or to consist of crystals formed in non-equilibrium conditions of the plume or particulates that originate from the single-crystal silicon target. Formation of crystals or the particulates may be reflected in the film morphology.

2.3 Experimental Setup

The laser ablation used in the research utilized a KrF excimer laser of λ = 248 nm. The average laser power 3 W with pulse duration of 8 nanosecond and repetition frequency 50 Hz [3]. The laser beam is collimated and focused to spot size of about 100 um onto the target with optics. As shown in Fig.2.2, the ablation is carried out in vacuum chamber. Cleaned single crystal silicon wafer is used as target. The native silicon oxide was removed with HF. The substrate is placed about 3 cm away from the target. Substrates of quartz and aluminum coated glass were used in the experiments. The ablation is done at pressure of 10^{-7} torr. A typical ablation time is about 15 minutes.
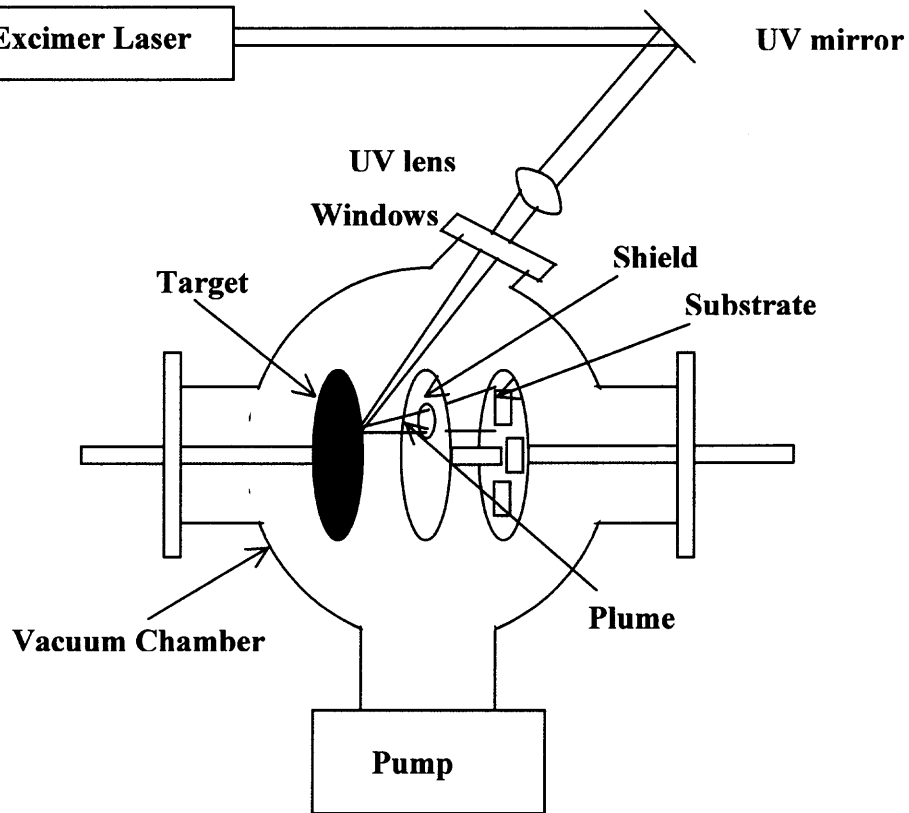
Fig.2.2: The schematic diagram of the laser ablation setup in this research

CHAPTER 3

REVIEW OF CHARACTERIZATION METHODS

3.1 Raman Spectroscopy

When light is scattered by a molecule or a crystal, most photons are scattered elastically and have the same energy (frequency) as the incident photons. This process is called Rayleigh scattering. However, it was observed by V. C. Raman in 1928 that a small fraction of photons (about 1 in $10^6 - 10^7$) were scattered with different energies from that of the incident radiation. This inelastic scattering process was then named as Raman scattering. The energy difference between the incident light and the Raman scattered light is related to the vibration energy of the molecule or the crystal lattice. A Raman spectrum is a plot of the scattered light intensity versus the energy difference. The Raman spectroscopy method has become a powerful analytical tool in chemistry and material science with the advance of the laser and detector technologies.

From a classic electromagnetic theory point of view, the Raman effect arises from the interaction of the incident photon with the electric dipole of the molecule. The interactions perturbs the electric field of the molecule. In quantum mechanics, the Raman scattering can be described as the excitation to a virtual state with energy lower than a real vibration state, as shown in Fig.3.1 [6]. The excitation will relax within less than 10^{-14} seconds with emission of a photon of different energy. At room temperature, most electrons are at ground state so the scattered photons will have lower energy than the incident photons, which is called Stokes scatter. A very small portion of molecules is in the vibration-excited state with energy higher than the ground state. The Raman scatter

9

Fig.3.1 Energy level diagram of the electron excitation in Raman scattering (a) Stoke's Raman scattering and (b) anti-Stokes Raman scattering.

by these molecules will result in photons with higher energy. It is called anti-Stokes scatter. The anti-Stokes line is always weaker than the Stokes line at room temperature because there are few electrons in the excited states than the ground states. The Raman shift that is the energy difference between the exciting and scattered photons is expressed
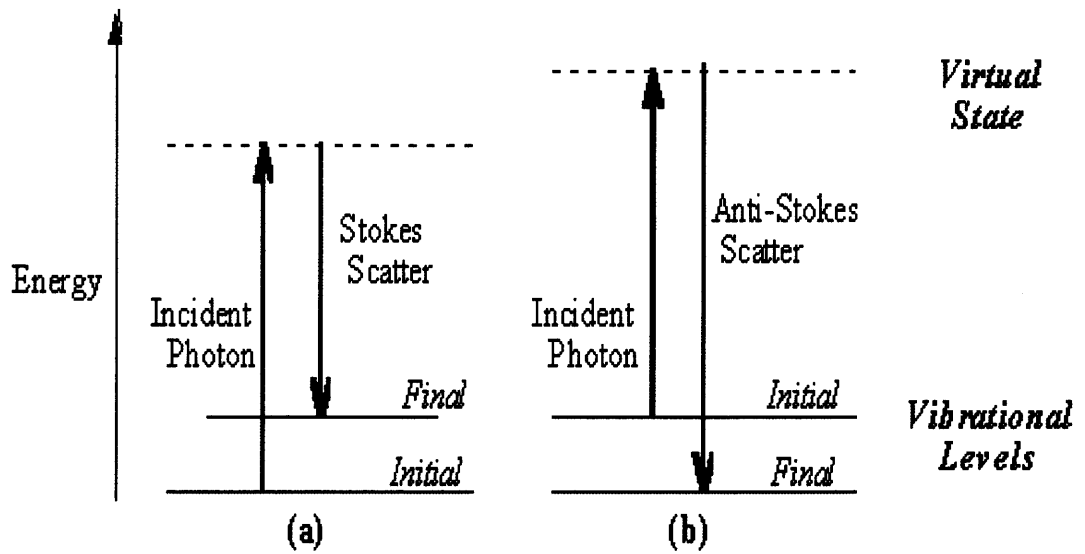
in wavenumber (cm^{-1}) as:

$$\overline{\nu} = \frac{1}{\lambda_{incident}} - \frac{1}{\lambda_{scattered}}$$

(3.1)

where the $\lambda_{incident}$ and $\lambda_{scattered}$ are the wavelengths of the incident and Raman scattered photons respectively.

For a molecule vibration to be Raman active, the polarizability of the molecule must be changeable during the vibration. Typical strong Raman scatters happen with bonds of distributed electron clouds. The energy of a vibration mode is decided by the molecule structure, the atomic mass, order of chemical bond, molecular substituents and hydrogen bonding etc. Applications of Raman spectroscopy are not limited to molecular identification. They can also be used to crystalline solids characterization. In crystal, the Raman scatter is the interaction with the lattice vibration or phonons. A phonon is Raman-active only when the first derivative of the polarizability to the vibration coordinate is non-zero. A phonon can be either Raman- or infrared-active dependents on the crystal symmetry. For certain crystal symmetry class, the Raman-active phonons can be calculated so the Raman measurement will reveal the information of the symmetry of the crystal lattice.

The Raman spectroscopy has been widely used in the study of the polymorphism and phase transformation of silicon [2]. The Raman spectrum of cubic silicon shows a single line at 520 cm^{-1} in absence of stress. The Raman line for the hexagonal silicon has been reported at around 510 cm^{-1} with an asymmetric broadened peak.

3.2 Scanning Electron Microscope

The scanning electron microscope (SEM) is a powerful tool for the structural and topographical characterization. Fig.3.3 is an illustration of the basic setup of a SEM. Electrons are generated from a thermionic, Schottky or field-emission cathode and accelerated toward the anode which is positive respect to the filament. The acceleration voltage can vary between as low as 0.1 keV to as high as 50 keV. The electron beam is then condensed by a condenser lens and is focused to a very fine spot on the sample through two- or three-stage of electron objective lens system. An electron probing beam of 1 to 10 nm of diameter with 10^{-9} to 10^{-12} A current is scanned on the sample surface. A scan coil system in front of the final objective lens generates a raster scan of the electron beam across the specimen by varying the coil voltage. At the same time, the varying voltage is also applied to the coil in the cathode-ray tube (CRT) which produces a scan pattern on the display synchronized with the electron beam scanning [7].

Several different interactions occur when the primary electron beam strikes the sample surface. They include both elastic and inelastic scattering and the final image has the contribution from a multiple large scale scattering and electron diffusion. However, the signals most commonly used include the secondary electrons (SE), the backscattered electrons (BSE) and X-rays. The SE imaging mode is the most common imaging mode in SEM. The secondary electrons are specimen electrons that obtain energy by inelastic collisions with primary electrons. The energy of SE is generally less than 50 eV. The advantage of SE mode is that these electrons can be detected at one side of the sample with a positive biased collector grid and a scintillator. The BSE trajectories are not affected by electrostatic field. BSE detector is mounted on the column with a large

collection angle. The contrast of the BSE image comes from the difference of the atomic number of different materials. The X-ray scattering can be used for both imaging and elemental analysis. For elemental analysis the X-rays are detected by energy- or wavelength-dispersive spectrometers.

The major advantages of the SEM over the optical microscope are the higher resolution, improved depth of focus and enhanced image contrast. Today, the advances of the computer and instrumental technologies have made the SEM very user friendly. Images of high quality can be taken by choosing correct working parameters such as the accelerating voltage, probe current and working distance. High accelerating voltage can produce smaller electron beam and improve the resolution. However, it will also enlarge the beam penetration and diffusion area. Other effects, like specimen chargeing and surface damage also increase at higher accelerating voltages. So finer structure images are typically obtained at lower accelerating voltage. The probe current will affect the image smoothness and resolution. A higher probe current helps the signal-to-noise ratio of the image but decreases the resolution. The working distance will influence the resolution and depth of field. Decreasing the working distance will improve the resolution sacrificing the depth of field.
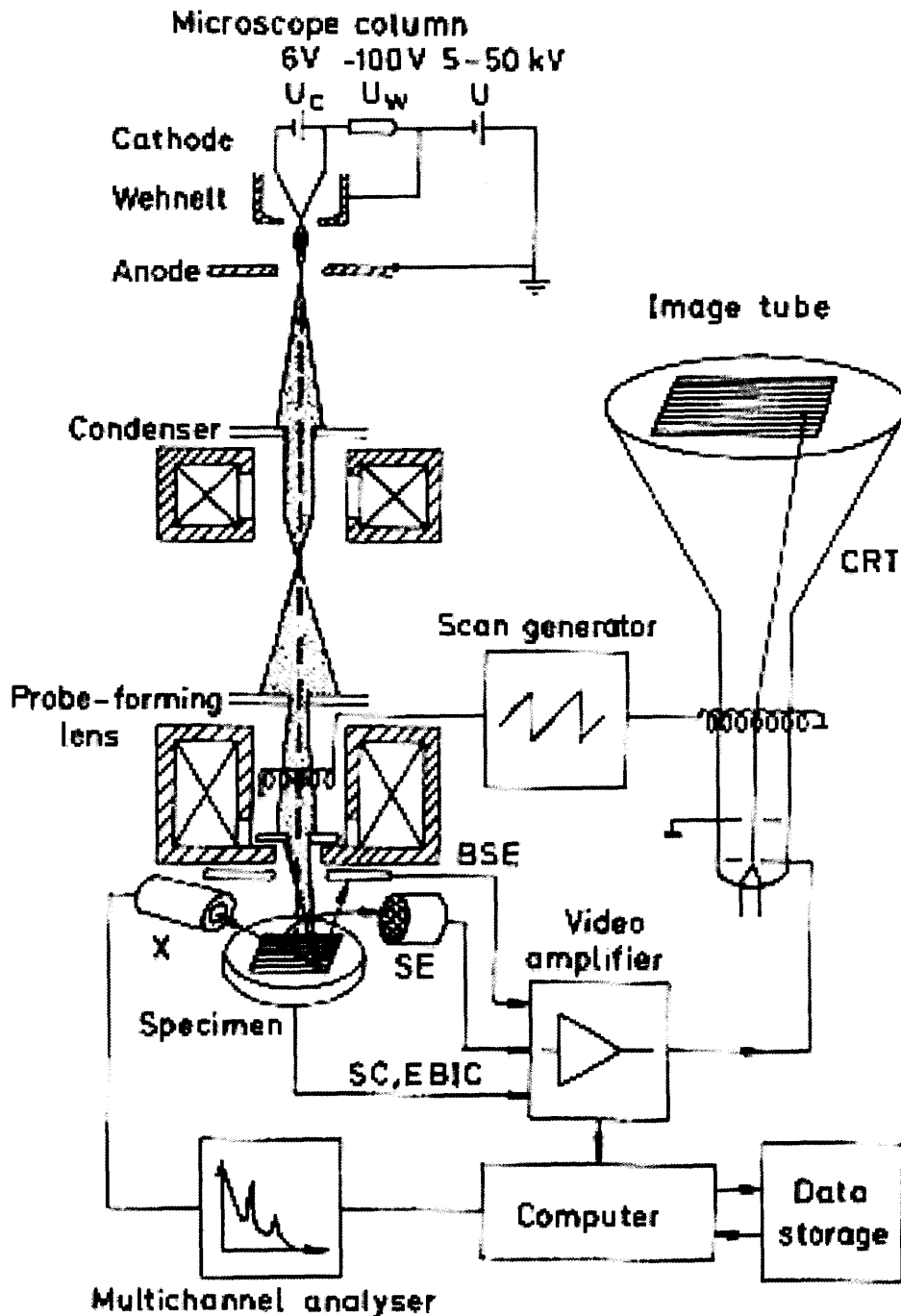
Fig.3.2 Schematic diagram that shows the principle of the scanning electron microscope [6]

3.3 Atomic Force Microscope

The atomic force microscope belongs to a group of instruments collectively known as scanning probe microscope (SPM) [7]. The SPM's are imaging tools that can approach resolution on the atomic scale. Material properties such as surface conductivity, elastic modulus, static charge distribution and magnetic fields can also be measured. There are two major types of SPM's, i.e. the scanning tunneling microscope (STM) and atomic force microscope (AFM). The STM, which was first developed by Nobel laureate Binning and Rohrer at IBM in 1982, operates by detection of the tunneling current with a sharp metal tip and thus is limited to imaging good electrical conductors. In 1986, Binning et al. developed the atomic force microscope that detects the force instead of the current. It enables the imaging on the atomic scale, of both conductors and insulators. The AFM offers advantages of three-dimensional imaging, requiring no specific sample preparation, and allows operation in vacuum, gas or liquid environment. Today, AFM has been extensively used in physics, materials science, biology and chemistry.

3.3.1 Principles of AFM

Fig.3.3 illustrates the basic operation principle of a contact mode atomic force microscope [8]. A micromachined soft cantilever with a sharp tip at one end is mechanically raster scanned across the sample surface. The cantilever deflects as the tip is attracted or repelled by the sample surface. The deflection of the cantilever beam is sensed by a laser-photodiode optical interferometer. A constant separation between the tip and the sample surface is maintained by piezoelectric feedback mechanism. By

recording the z-direction movement of the raster scanner with respect to the x-y position, the topographic image of the sample surface is generated.

The contact-mode AFM has several drawbacks. First, the sharp tip can damage the surface of soft samples such as polymers or biological samples. Second, small samples such as DNA or cells are often destroyed or pushed out of the scanning field by the rastering tip. To overcome above-mentioned issues, tapping mode AFM has been developed [9]. Under tapping-mode operation, the cantilever beam oscillates at its resonant frequency while the tip is scanned across the sample surface. The tip touches the surface only at the bottom of each oscillation and thus prevents the damage or pushing of the sample. A constant distance is also maintained between the tip and the sample surface in tapping-mode AFM. It can be used for both dry and liquid samples.

3.3.2   Artifacts in AFM Imaging

There are four major sources for AFM artifacts, i.e. from the probe, the scanners, the image processing and the environmental vibrations [10]. The AFM image is the convolution of the probe geometry and the sample surface features. To avoid the probe artifacts, the probe size needs to be smaller than the features under measurement. A broken or chipped tip will lead to distorted AFM image. An AFM scanner is typically made of piezoelectric ceramics, which displays nonlinearity and hysteresis. All atomic force microscopes need calibration in both x-y and z-direction to generate accurate images on the computer screen. The hysteresis of the scanner can cause edge overshoot. The image processing artifacts are generated when the software is not used properly. A

typical error is that the image is over-touched. The environmental vibration can cause the

oscillation artifacts in AFM imaging. The vibration source can be from floor or acoustic.
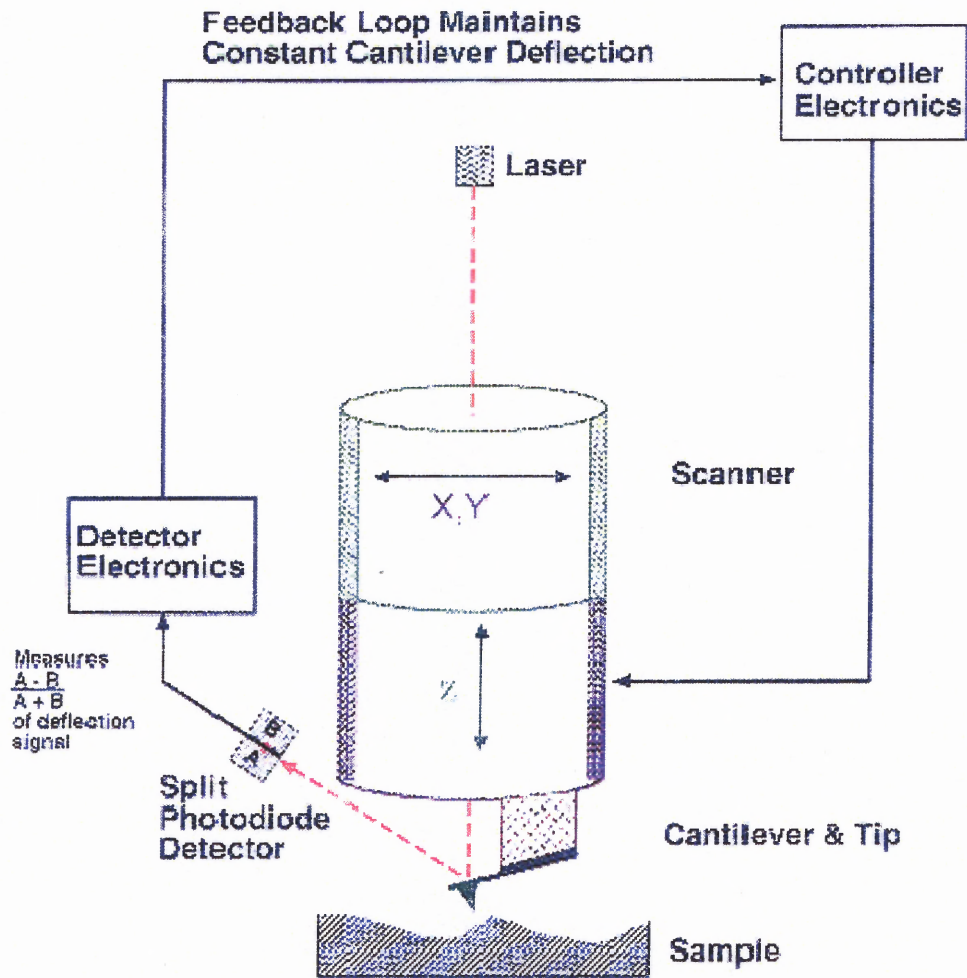

Fig.3.3 Schematic illustration of the principle of atomic force microscope [9]

3.4 Nanoindentation

3.4.1 Introduction

Although mostly used as an imaging instrument, the atomic force microscope can also be used to test the mechanical or electrical properties of materials. As an example, the Young's modulus and the hardness of a solid sample can be determined by so-called nanoindentation method with AFM [11]. In this section, the principle and the method for interpretation of the nanoindentation data are briefly discussed.

Indentation testing is a method of testing mechanical properties such as elastic modulus and hardness of a material by touching it with a second material whose corresponding mechanical properties are already known. The nanoindentation is an indentation test that is performed at a penetration depth scale in nanometers (10^{-9}), compared with the dimension of microns (10^{-6}) or millimeters (10^{-3}) in the conventional indentation tests. It means that nanoindentation test can apply low enough forces to give penetration depths less than 10% of the thin film thickness so as to avoid influence from the substrate. Another unique feature of nanoindentation testing is its indirect measurement of the contact area (the area of contact between the indenter and the specimen). In conventional indentation tests, the area of contact is calculated from direct measurements of the dimensions of the residual impression left on the specimen surface upon the removal of the load. In nanoindentation tests, the size of the residual impression is of the order of microns, which is too small to be measured directly. The area of contact is determined by measuring the depth of penetration of the indenter of the known shape.

In nanoindentation test, an indenter is placed in contact with the flat surface of the specimen with a steadily increasing load. Both load and depth of penetration are recorded

at each load increment. After the maximum point, the load is steadily removed and the penetration depth is recorded. The loading part of the indentation cycle may consist of an initial elastic contact, followed by a plastic flow or yield within the specimen at high loads. Upon unloading, if yield has occurred, the load-displacement data follow a different path until at zero applied load; a residual impression is left in specimen surface. The hardness and the elastic modulus of the specimen material are calculated from the maximum depth of penetration for a particular load, together with the slope of the unloading curve measured at the tangent to the data point at maximum load.
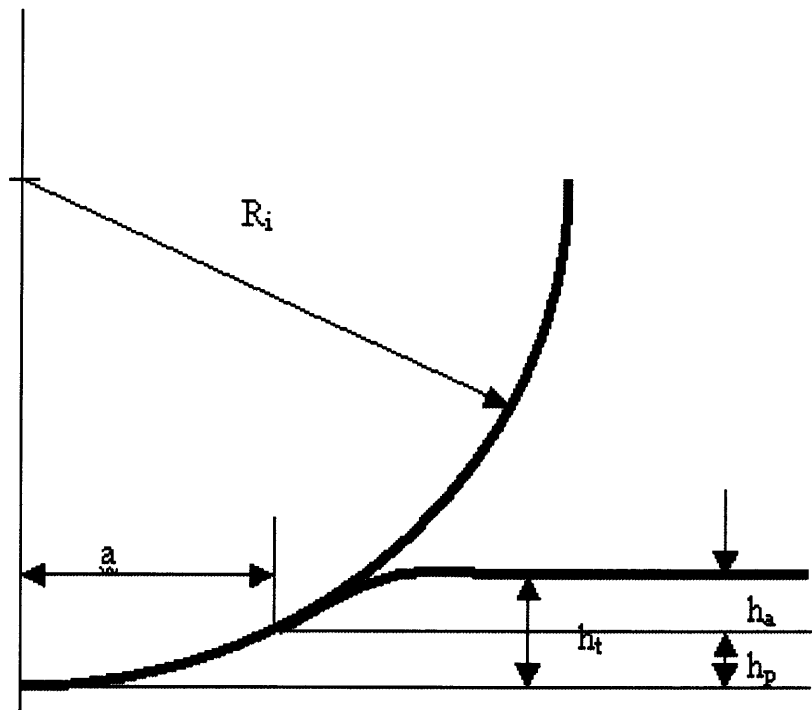
Fig.3.4 Schematic of elastic contact between a rigid indenter and a flat surface

3.4.2 Elastic Contact Mechanics [11]

Let's consider a situation when a rigid spherical indenter is brought to elastic contact with a flat surface (Fig.3.4). The stresses and deflections arising from the contact between two elastic solids are of particular interest to those undertaking indentation testing. The relationship between the radiuses of the contact circles a and the load P is:

$$a^3 = \frac{3PR}{4E^*} \tag{3.2}$$

Where R is the radius of the rigid sphere indenter; E^* is the combined modulus of the indenter and the specimen, which is expressed as:

$$\frac{1}{E^*} = \frac{(1-v^2)}{E} + \frac{(1-v'^2)}{E'} \tag{3.3}$$

The deflection h of the original free surface in the vicinity of the indenter is given by:

$$h = \frac{1}{E^*}\frac{3}{2}\frac{P}{4a}\left[2 - \frac{r^2}{a^2}\right] \qquad r \leq a \tag{3.4}$$

It can be calculated that $h_a = h_p = h_t/2$, where ha and ht are the depth at r = a and r = 0. The distance of mutual approach of distant points in the indenter and specimen is:

$$\delta^3 = \left[\frac{3}{4E^*}\right]^2 \frac{P^2}{R} \tag{3.5}$$

Combining eq.3.2 and eq.3.5 then we get:

$$\delta = \frac{a^2}{R} \tag{3.6}$$

For the case of a non-rigid indenter, δ becomes the total depth of penetration h_t beneath the specimen free surface:

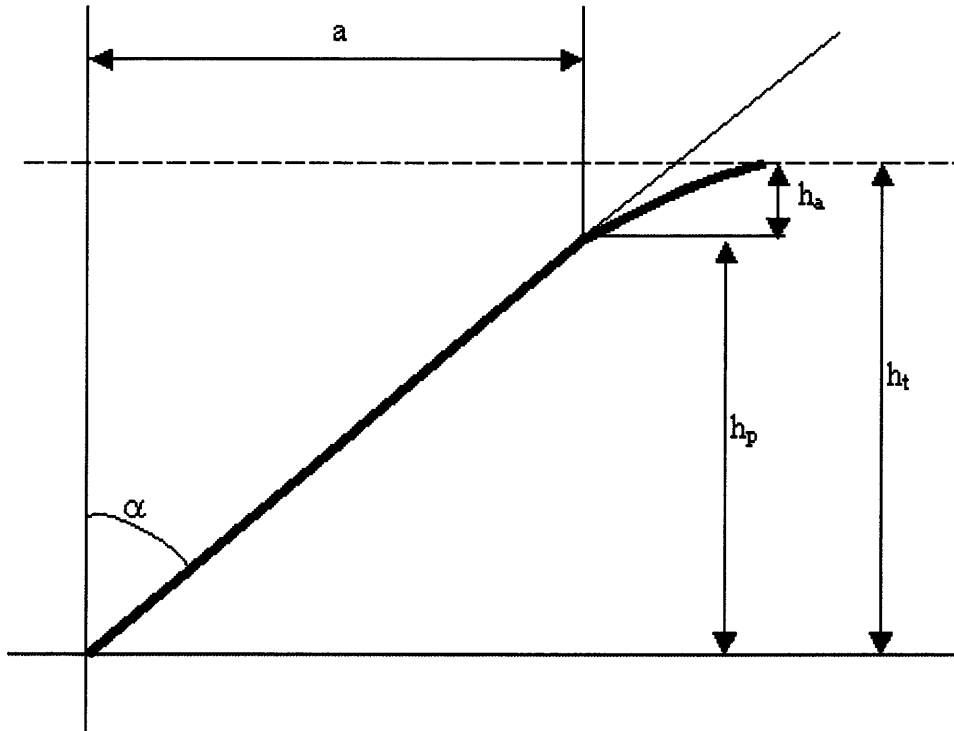$$P = \frac{4}{3}E^* R^{1/2} h_t^{3/2} \tag{3.7}$$

Fig.3.5 Schematic of contact by conical indenter
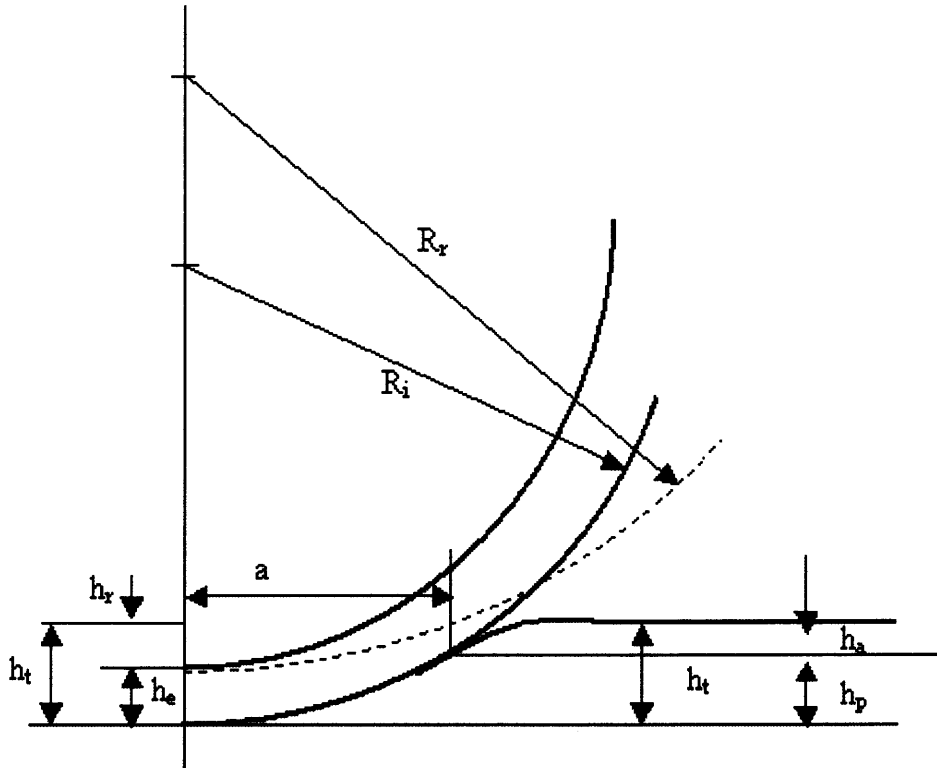
Fig.3.6 Schematic shows loading a preformed impression of radius R_r with a rigid indenter of radius R_i
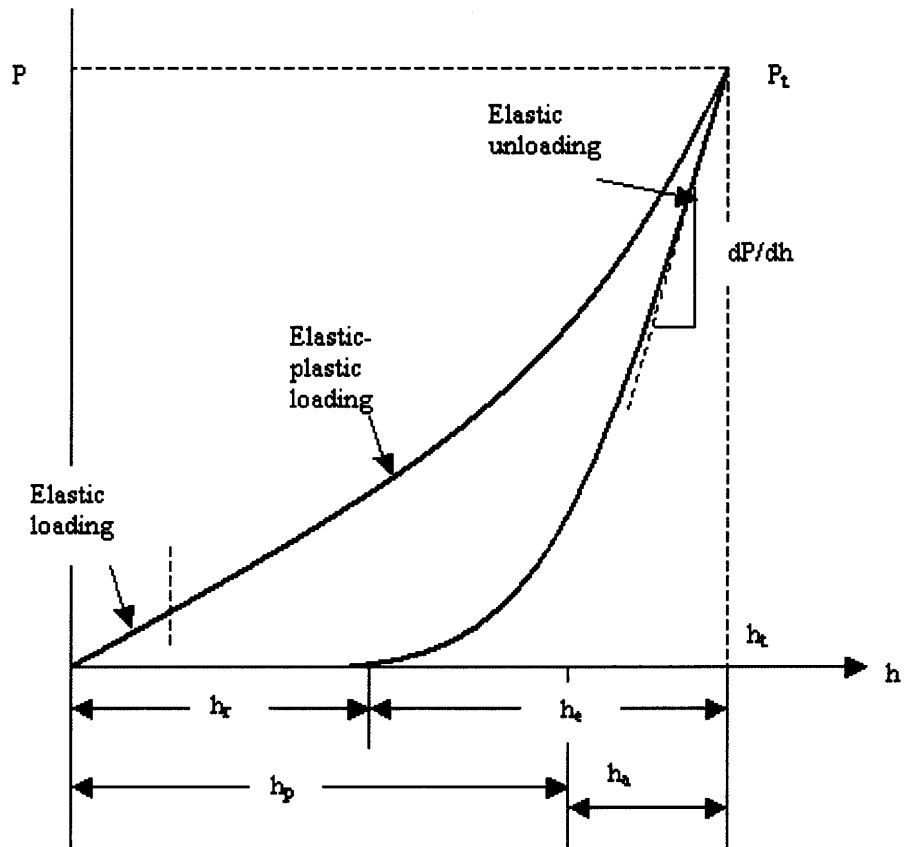
Fig.3.7 Load vs. displacement curve for an elastic-plastic specimen loaded with a spherical indenter.

Consider the loading of an initially flat specimen with a spherical indenter. Upon loading, there may be an initial elastic response at low loads followed by elastic and plastic deformations within the specimen material at increased loads. With reference to Fig3.4 the depth of penetration of a rigid spherical indenter beneath the original specimen free surface is h_t at full load p_t. When the load is removed assuming no reverse plasticity, the unloading is elastic and at complete unload, there is a residual impression of depth h_r.

If the load P_t is reapplied, then the reloading is elastic through a distance $h_e = h_{t}$-h_r according to the equation 3.2:

$$P = \frac{4}{3} E^* R^{1/2} h_e^{3/2}$$ (3.8)

We use multiple-point unload method to analyze the data. The multiple-point unload method uses the slope of the tangent to the initial unloading to determine the depth of contact h_a and then h_p. From eq.3.5 and 3.8, we get:

$$\frac{dP}{dh} = 2 E^* R^{1/2} h_e^{1/2}$$ (3.9)

Solving above equation we have:

$$h_a = \left(\frac{\pi - 2}{\pi} \right) h_e$$ (3.10)

Substituting eq.3.9 into eq.3.8, we get:

$$P = \frac{2}{3} \frac{dP}{dh} h_e^{1/2}$$ (3.11)

Thus,

$$h_e = \frac{3}{2} P \frac{dh}{dP}$$ (3.12)

With reference to fig3.6, fig3.7, the unloading from ht to hr is assumed to be elastic, and for a spherical indenter, the Hertz equations show that the depth of the circle of contact h_a beneath the specimen free surface is half of the elastic displacement h_e, that is: $h_a=h_e/2$. For a rigid spherical indenter, Hertz showed that elastic displacement is given by:

$$h_e = \frac{a^2}{R} \tag{3.13}$$

from eq.3.13 and eq.3.9 we get:

$$E^* = \frac{dP}{dh} \frac{\sqrt{\pi}}{\sqrt{A}} \frac{1}{2} \tag{3.14}$$

As for a conical indenter, similar equations apply where the radius of circle of contact is related to the indenter load by:

$$P = \frac{\pi a}{2} E^* a \cot \alpha \tag{3.15}$$

$$h = \left[\frac{\pi}{2} - \frac{r}{a}\right] a \cot \alpha \qquad r \le a \tag{3.16}$$

$$P = \frac{2E^* \tan \alpha}{\pi} h_t^2 \tag{3.17}$$

In nanoindentation testing, pyramidal indenters are generally treated as conical indenters with a cone angle that provides the same area to depth relationship as the actual indenter in question.
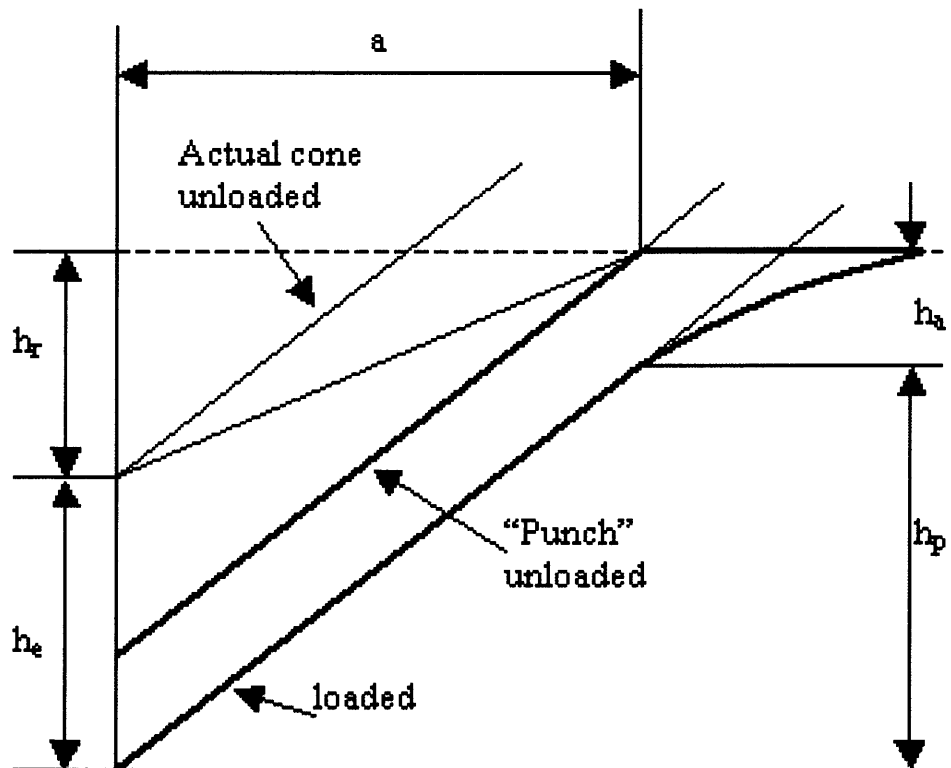
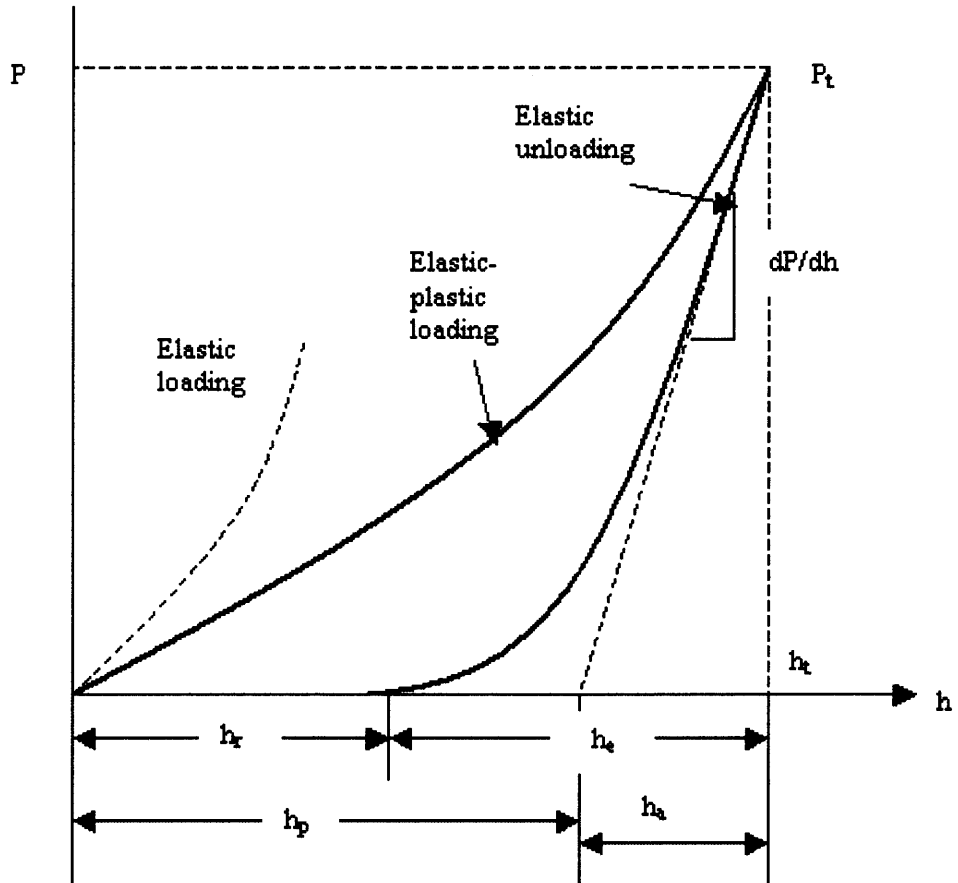**Fig.3.8** Schematic of indenter and specimen at full load and unload with a conical indenter

Fig.3.9 Load-displacement curve for elastic-plastic loading followed by elastic unloading.

3.4.3 Nanoindentation with SPM

We did nanoindentation tests in New Jersey Institute of Technology using Digital Instruments SPM. The forces involved when indenting are typically in the range of 1-100 uN for a standard cantilever. The indentation probe consists of a diamond tip mounted to stainless steel cantilever. The cantilevers have spring constants higher than the typical cantilevers used for imaging, which allows the application of forces large enough to indent or scratch a sample surface. Imaging is performed non-destructively by the patented TappingMode[TM] technique. Thus, the same probe used for testing can also be used to locate the area of interest.
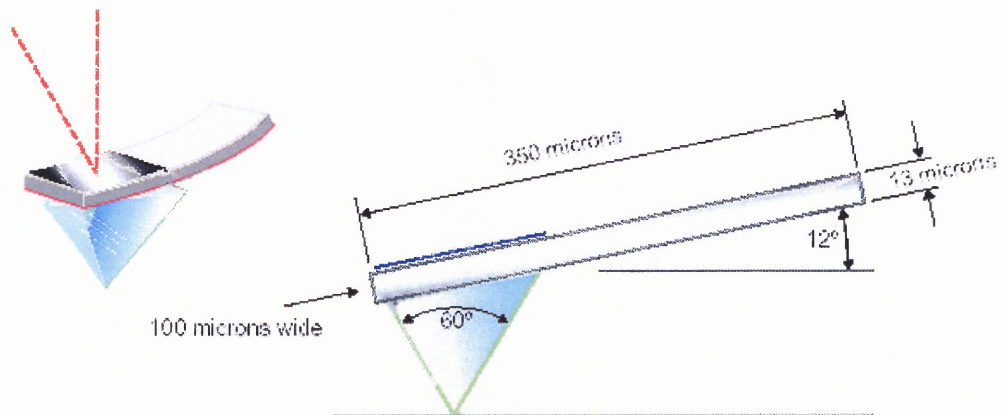

Fig.3.10 Schematic of the indenter tip used in the experiment.

Table 3.1 Specifications of the probe used in this research

Item	Value
Force (or Spring) Constants	210 N/m
Resonant Frequency	~ 45 kHz
Nominal Tip Radius of Curvature	< 25 nm
Cantilever Length	356 µm
Cantilever Configuration	Single Beam
Reflector	Silicon Mirror
Cantilever Material	Stainless Steel
Tip Material	Diamond
Tip Apex Angle	60°

The indenter has a face angle of $\theta = 19.47°$, the relationship between the projected area A of the indentation and the depth h_p beneath the contact is:

$$A = 3\sqrt{3}h_p{}^2 \tan^2 19.47 = 0.65 h_p{}^2 \qquad (3.18)$$

Once h_p is found, the projected area of contact is calculated and the harness computed from

$$H = \frac{P}{A}$$

Upon unloading, the contact is elastic and the relationship between the load and the depth of penetration for a cone is given by eq.3.16:

$$P = \frac{2}{\pi} E^2 h_e{}^2 \tan\alpha' \qquad (3.19)$$

where a' is now the combined angle of the indenter and the residual impression. The normal displacement h of points on the surface beneath the indenter is a function of the radial distance r from the axis of symmetry and is given by:

$$h = \left[\frac{\pi}{2} - \frac{r}{a}\right] a \cot\alpha' \qquad r \leq a \qquad (3.20)$$

As shown in Fig3.8 and Fig3.9, as the indenter is unloaded, the tip of the indenter (r=0) moves through a distance h_e and the edge of the circle of contact with the specimen surface (r=a) moves through a distance h_a. Using eq.3.20, at the load P_t the displacements h_e and h_a are:

$$h_e = \frac{\pi}{2} a \cot\alpha' \qquad (3.21)$$

$$h_a = \left[\frac{\pi}{2} - 1\right] a \cot\alpha' \qquad (3.22)$$

And then we get:

$$h_a = \left[\frac{\pi - 2}{\pi}\right] h_e \tag{3.23}$$

And

$$h_t = h_p + h_a \tag{3.24}$$

We use multiple-point unload method to analyze the data. The multiple-point unload method uses the slope of the tangent to the initial unloading to determine the depth of contact h_a and then h_p. From eq.3.19, the slope of the elastic unloading is given by:

$$\frac{dP}{dh} = 2\frac{2E^* \tan\alpha'}{\pi} h_e \tag{3.25}$$

Then

$$P = \frac{1}{2}\frac{dP}{dh} h_e \tag{3.26}$$

Substituting eq.3.26 into eq.3.23 , we get:

$$h_a = \left[\frac{2(\pi - 2)}{\pi}\right]\frac{P_t}{dP/dh} \tag{3.27}$$

from which h_p can be found from eq.3.24 and the projected area of contact A from eq. 3.18 and the combined modulus E* from eq.3.14. Oliver and Pharr, found that the intercept correction for pyramid tip is 0.75 to account for the inevitable rounded tip of a real indenter. Finite element calculations for indentations formed with flat-ended punches of triangular cross sections yield a correction factor β equal to 1.034 for a pyramid indenter.

$$E^* = \frac{dP}{dh}\frac{1}{2h_P}\frac{1}{\beta}\sqrt{\frac{\pi}{0.65}} \tag{3.28}$$

3.5 I-V Characterization by STM

The scanning tunneling microscopy (STM) measures the "tunneling current" between the probe and the sample to sense the topography of the sample. The operation relies on the mechanism of electrons quantum tunneling through a potential barrier. In practice, a metal tip is brought very close (on the order of an angstrom) to the surface of the sample. When a bias voltage is applied to the tip or sample, the electrons are attracted by the positive side of the potential. The gap between the tip and the sample becomes a finite barrier potential for electrons that are nearly free. Under the quantum effect, electrons begin to tunnel through the barrier. The tip is then restered across the two dimensional surface of the sample while the current is recorded. The current can be used to gather information about the topography and electronic structure of the surface of the sample.

In this research, the STM was used to study the current-voltage (I-V) characterizations of laser-ablated silicon. The samples consist of hexagonal silicon islands with featureless nanoclusters between them. The advantage of STM is that the tip can be precisely located on the top of the hexagonal silicon islands which are of microns scale. The Digital Instrument multimode SPM was used in the experiments. The STM probe, a sharp tip less than 0.012" in diameter made of platinum iridium alloy, is positioned a few atomic diameters above a sample which is positively biased with respect to the tip. At a distance under 1 nm, a tunneling current will flow from sample to tip. In operation, the bias voltages typically range from 10 to 1000 mV while the tunneling currents vary from 0.2 to 10 nA. The tunneling current changes exponentially with the tip-sample separation, typically decreasing by a factor of two as the separation is increased 0.2 nm.
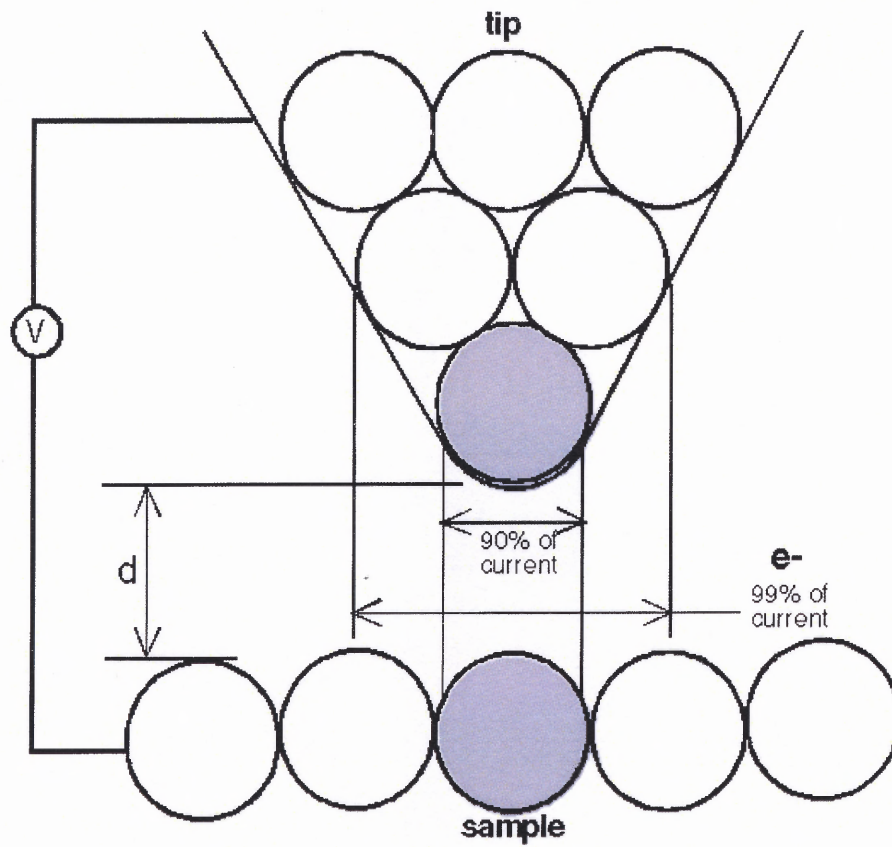
Fig.3.11 Schematic shows the tunneling effect between the specimen and STM tip.

CHAPTER 4

EXPERIMENTAL RESULTS AND DISCUSSION

4.1 Laser Ablation of Silicon

Thin films in this research were deposited by laser ablation utilizing a KrF excimer laser (Lamda Physik model EMG 102) of $\lambda = 248$ nm wavelength. The average laser power is 3 W with pulse repetition frequency 20 Hz. The laser beam is collimated and focused to spot size of about 100 um onto the target with a f = 15 cm ultraviolet lens. The ablation was carried out in a vacuum chamber. Cleaned single crystal <100> silicon wafer was used as target. The native silicon oxide was removed with HF acid and followed by rinsing by water and methanol. The substrate is placed about 3 cm away from the target. The chamber was evacuated to pressure of 5×10^{-7} torr by turbo-molecular pump. A typical ablation time was about 10 minutes. Two types of substrates were used in the laser ablation of the silicon, i.e. quartz and aluminum coated quartz. The substrates were cleaned with acetone and methanol. The aluminum coating on the quartz was done by evaporation. In the laser ablation, the laser beam was rastered across the target surface and the target was rotated in order to avoid drilling a hole into the target. Both target and substrate were maintained at room temperature at the start of the experiment [3].

Some of the deposited samples were annealed at different temperatures and annealing ambient. One condition was 550 °C in argon; another condition was 550 °C in argon with 4% hydrogen. A variety of properties of the as-deposited and annealed samples were studied as presented in the next section.

33
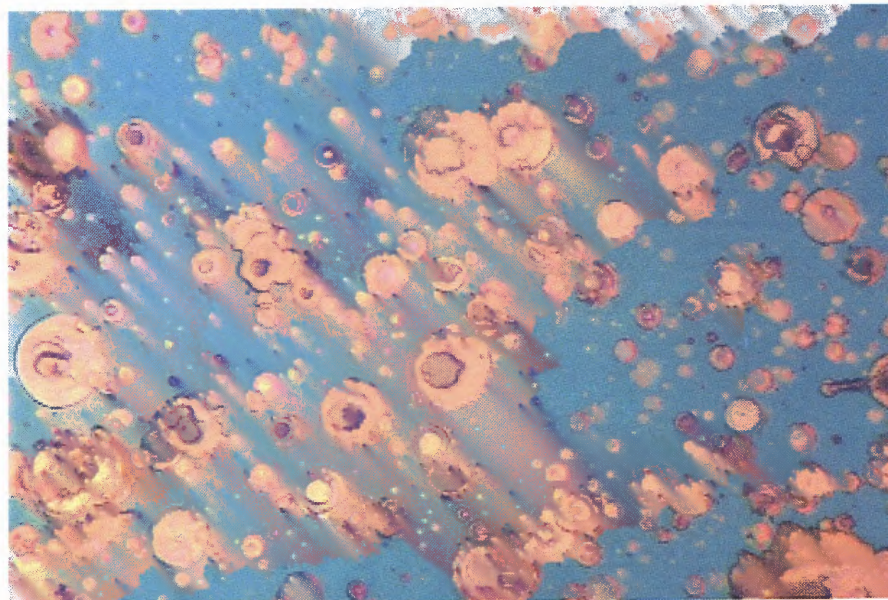
(a)
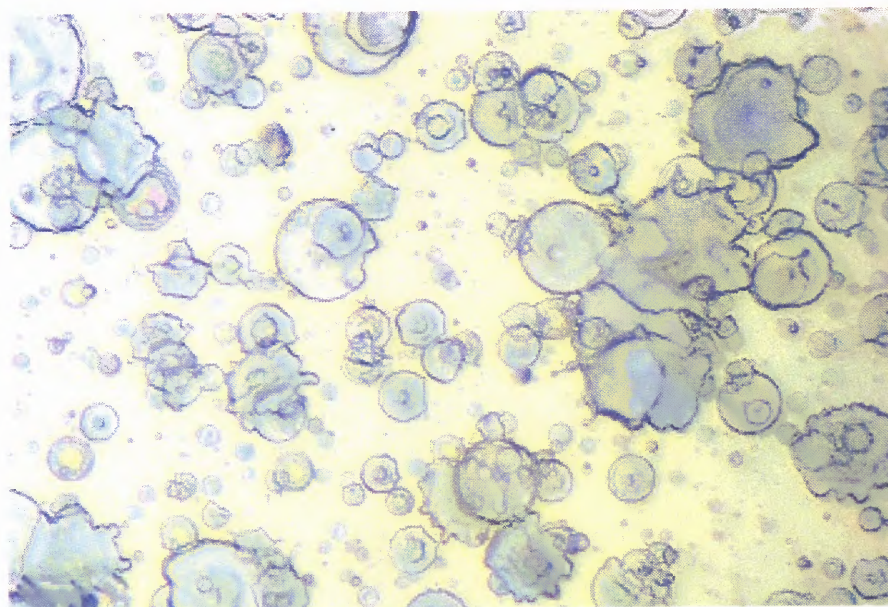
(b)

Fig.4.1 Optical micrographs of the silicon film deposited by laser ablation (a) on aluminum; (b) on quartz.

4.2 Experimental Characterization

Optical micrograph show that the as-deposited samples consist of crystalline droplets with size of 5 – 25 um scattered among a smooth featureless matrix. The films on both quartz and aluminum have similar morphology, as shown in Fig.4.1. The splash patterns of the droplets suggest that they were in molten state when they arrived at the substrate. The deposited silicon films were subjected to several experimental characterizations, including micro-Raman spectroscopy, the topography characterizations by AFM and SEM, mechanical tests by nanoindentation method, and electrical measurements using STM and contact probe measurement.

4.2.1 Raman Spectroscopy

The Raman spectra were taken with a confocal scanning micro-Raman spectrometer. Figures 4.2 and 4.3 are the results obtained on the films on aluminum and quartz substrates. The Raman spectrum taken on the silicon target shows a Raman signal at 520 cm^{-1} [Fig.4.2(a), 4.3(a)]. The Raman shifts for the crystalline islands are 514.38 cm^{-1} and 517 cm^{-1} for films on aluminum and quartz substrate, respectively [Fig.4.2(b), 4.3(b)]. Based on the previous study, we assign those Raman lines to the hexagonal symmetry [3]. Theoretically, the Raman spectra for the crystalline consist of 3 lines that overlap. For the annealed samples, the one annealed in argon shows a Raman shift at 520 cm^{-1} [Fig.4.2(c)], which suggests that most of the hexagonal silicon converts back to cubic silicon. On the other hand, the film annealed in Ar + 4% H$_2$ doesn't show much change [Fig.4.2(d)].
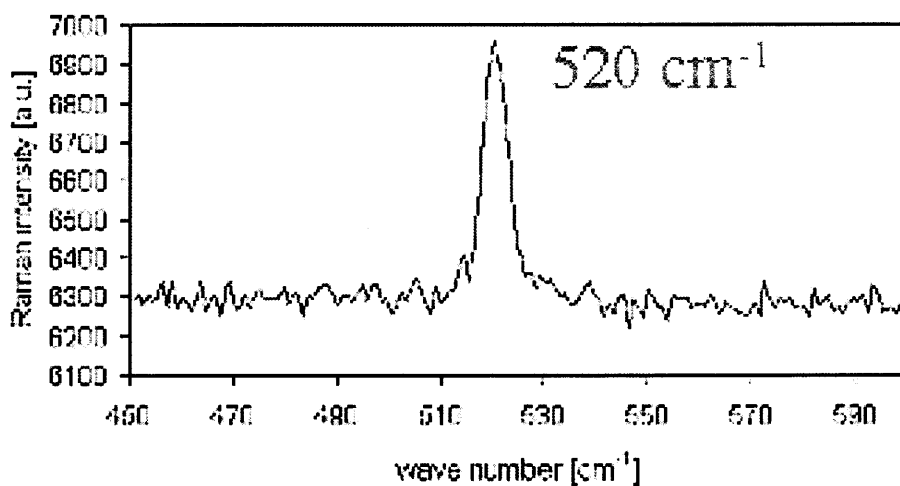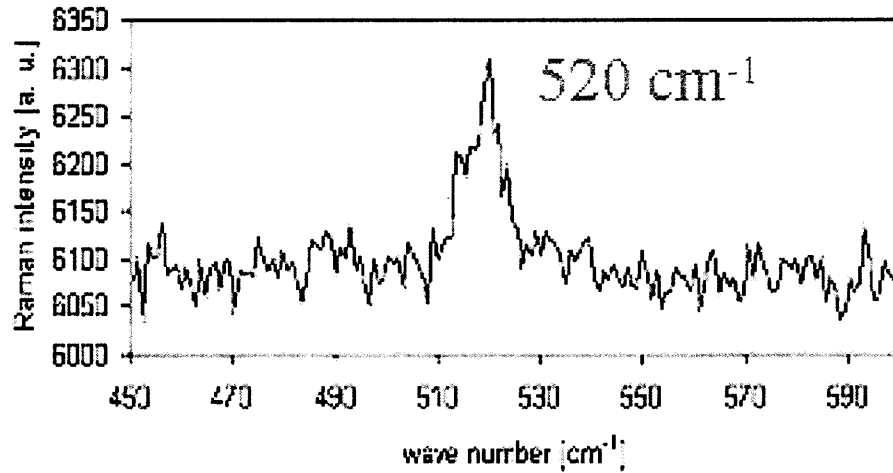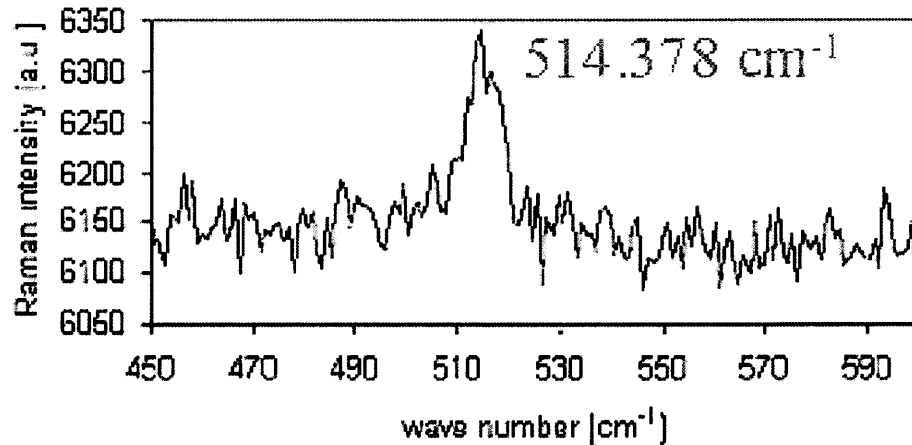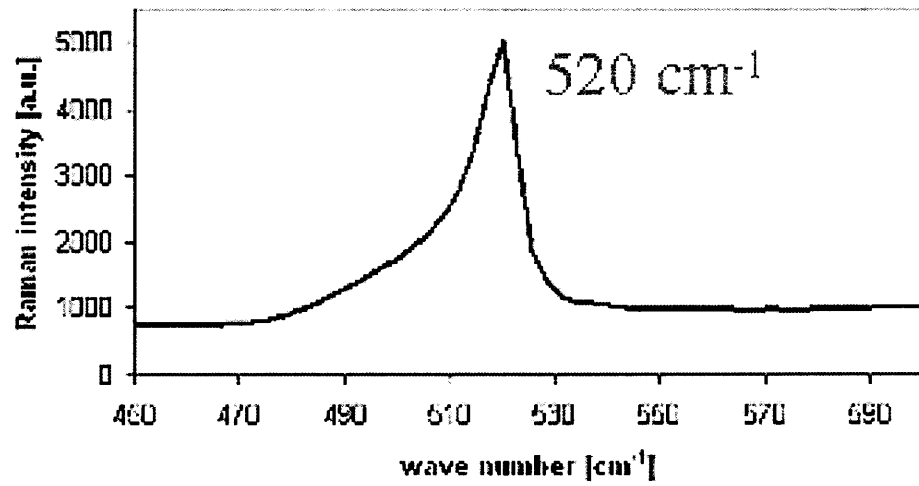
(a)
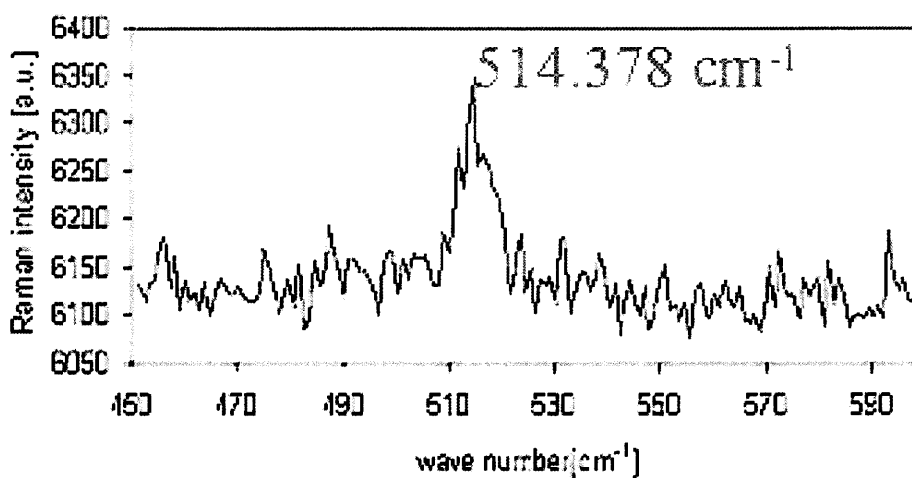
(b)

Fig.4.2 (a) - (b)

(c)

(d)

Fig.4.2 Raman spectra results (a) silicon target; (b) as deposited silicon film; (c) sample after annealing at 550 °C in Ar; (d) sample after annealing at 550 °C in Ar + H_2. All samples are on aluminum coated quartz substrate (The noise observed in the background rather than the spectra structure is responsible for the complex shape of peaks of 520 cm^{-1} and 514.378cm^{-1}.)
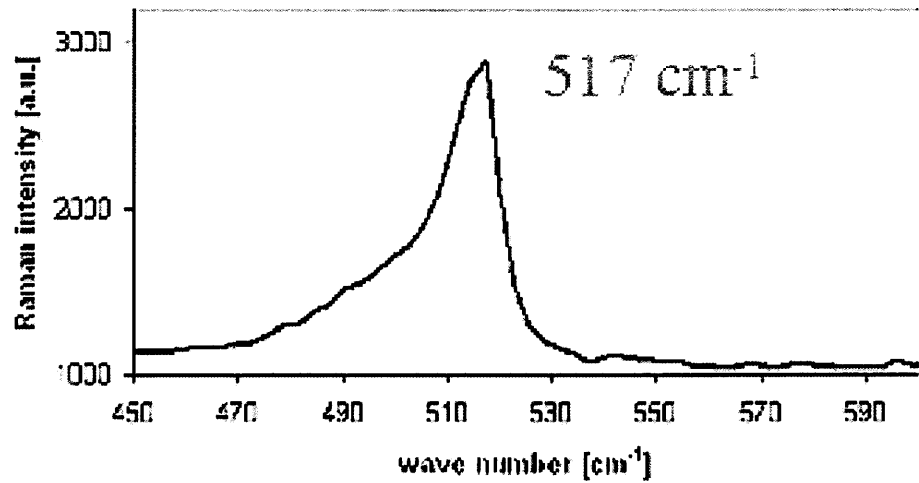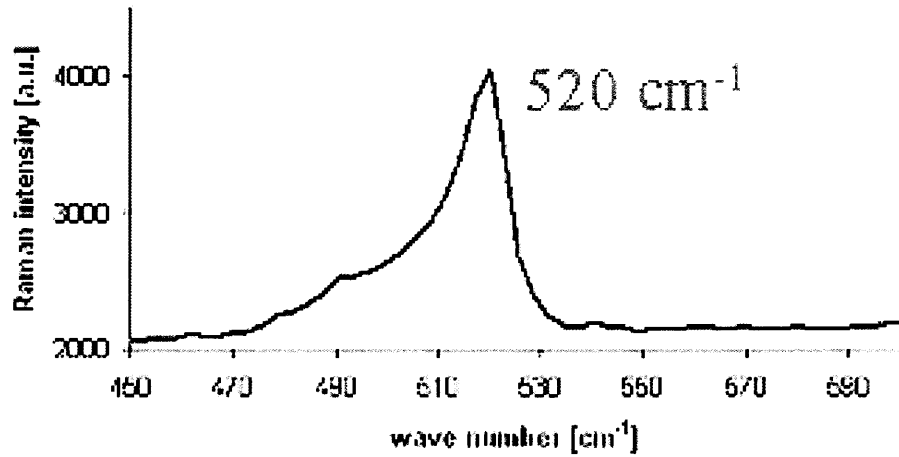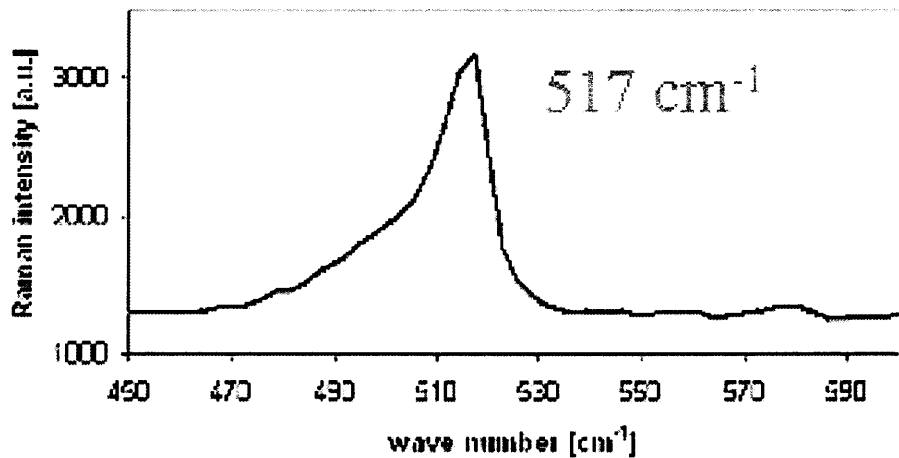
(a)

(b)

Fig.4.3 (a) – (b)

(c)



(d)

Fig.4.3 Raman spectra results (a) silicon target; (b) as deposited silicon film; (c) sample after annealing at 550 °C in Ar; (d) sample after annealing at 550 °C in Ar + H_2. All samples are on quartz substrate (Fig.4.3 was taken with a different Raman spectroscopy from Fig.4.2. The asymmetric shape of the peaks with the shoulders on the left side is an artifact of the instrument).

4.2.2 SEM and AFM

The topographical investigations were carried out with scanning electron microscope and atomic force microscope. The SEM study was done on a Leo 1530 field emission SEM. The operation of the SEM was controlled with LEO-32 user interface windows software. The SEM image was taken with an acceleration voltage of 2 KeV and working distance 3 to 4 mm. Figure 4.4 shows the micrographs of the deposited silicon films on aluminum and quartz substrates respectively. An enlarged view of the crystalline island microstructure is shown in Fig.4.5. The islands have splash patterns, which suggest that they were formed from a molten state.

The AFM measurements were carried out with Digital Instruments Nanoscope III with a piezoelectric tube scanner. The AFM images were taken under tapping mode. Figure 4.6 shows the AFM image of the droplet structure. The AFM results are consistent with the SEM images. These topographical characterizations confirm the morphology observed by optical microscope with more details.

The topography of the silicon films after annealing under different conditions was also examined. Figure 4.7 shows the SEM pictures of the samples annealed in argon and argon with 4% hydrogen, respectively. As expected, there is no obvious change in the film topography before and after annealing at the relatively low temperature of 550 °C.
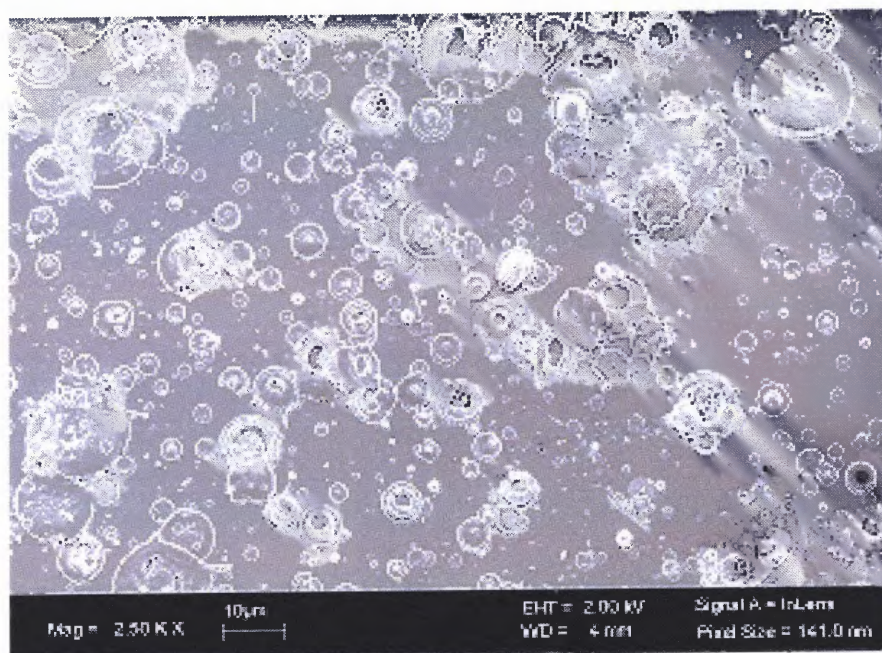
(a)

(b)

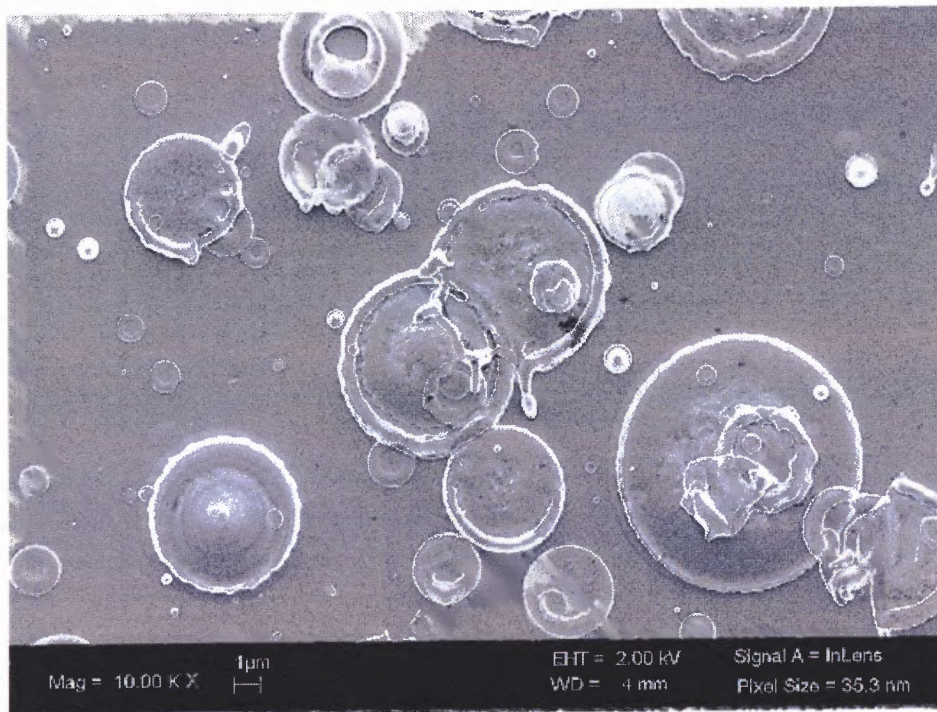**Fig.4.4** SEM micrographs of as deposited silicon films (a) on aluminum; (b) on quartz.

Fig.4.5 Enlarged view of the droplets structure of the laser ablated silicon film on quartz

obtained with SEM
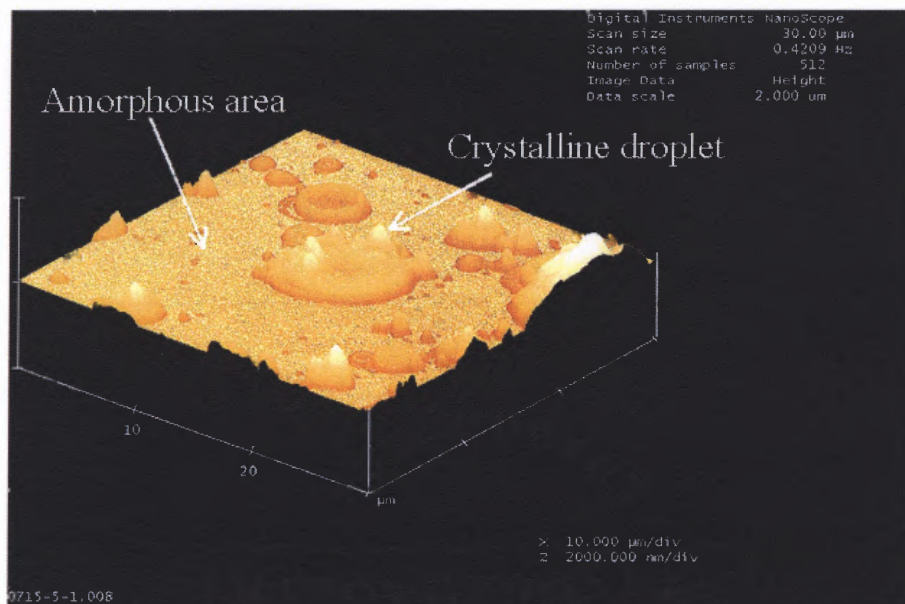
(a)
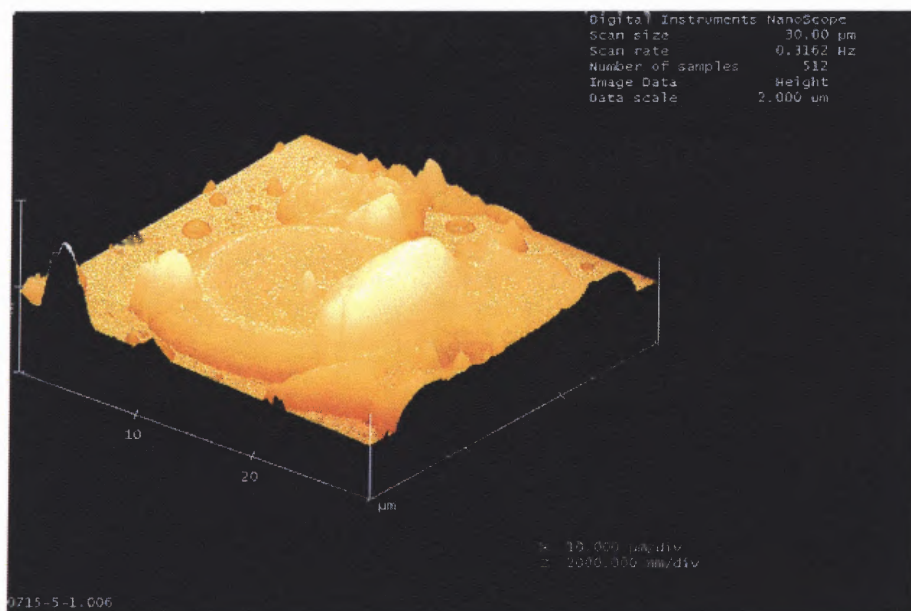
(b)

Fig.4.6 AFM images of the silicon droplets by laser ablation (a) on aluminum; (b) on quartz

(a)

(b)

Fig.4.7 SEM images of silicon film on aluminum after annealing at 550 ^{o}C (a) in Ar; (b) in Ar + 4% H_2

(a)

(b)

Fig.4.8 SEM images of silicon film on quartz after annealing at 550 ^{o}C (a) in Ar; (b) in Ar + 4% H$_2$

4.2.3 Nanoindentation Results

The nanoindentation tests were performed with the Digital Instruments Nanoscope. A diamond tip with pyramid shape was used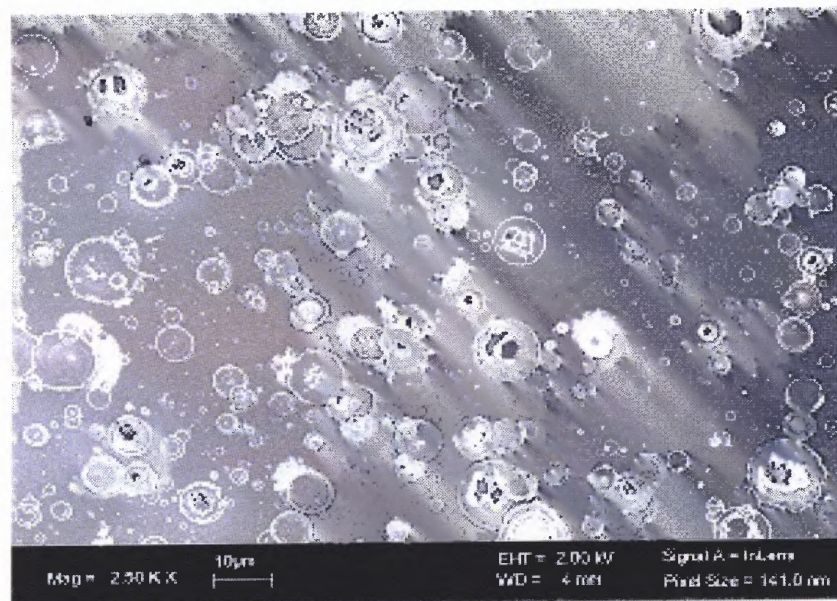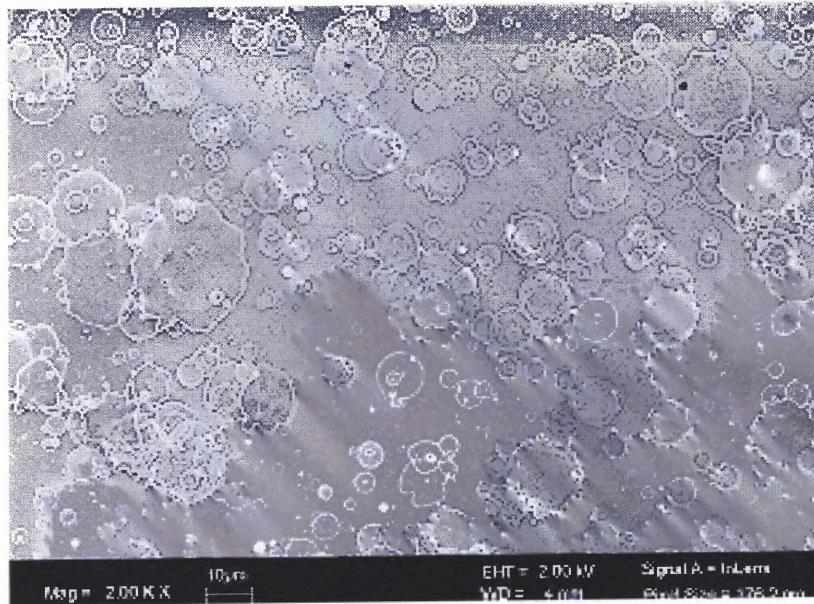. The indentation was made by forcing the tip into the sample surface until the required cantilever deflection is reached. The tip is then lifted to its initial Z position above the sample surface. A plot of the cantilever deflection versus the displacement in the Z direction, called a force plot, was recorded. To calculate the force applied to the sample during indentation it is necessary to first measure the cantilever sensitivity. The cantilever sensitivity is the cantilever deflection signal versus the voltage applied to the Z piezo, which was measured from the force plot captured. It is accurate to measure the cantilever sensitivity on a very hard sample, since there is little surface penetration. The sapphire sample was used to measure the cantilever sensitivity in this research. Once the sensitivity is known, the force of indentation is determined from Hooke's Law $F= kx$ where k is the spring constant and x is the cantilever deflection.

The nanoindentation tests have been carried out on samples of as-deposited silicon film, and the films after annealing at 550 °C in argon and argon with hydrogen. All the samples are on quartz substrates. Figures 4.9 to 4.11 show the nanoindentation results. First, a curve shows the relationship between the loading force and the vertical movement of the diamond tip. Then the curve was converted to the loading-unloading curve. From the loading-unloading curve, the Young's modulus was calculated using the procedure presented in chapter 3. Table 4.1 listed the Young's modulus obtained from the nanoindentation tests for the as-deposited and annealed silicon films.

Table 4.1 Young's modulus results by nanoindentation

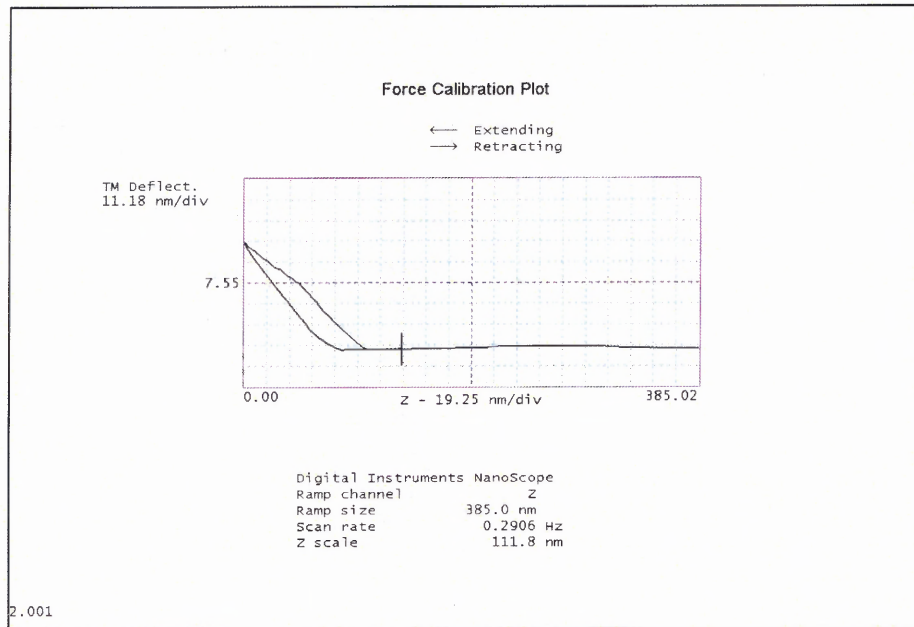| Measurements	Young's modulus (GPa)					
	1	2	3	4	5	Average Value
As-deposited Hexagonal silicon film	120	130	122	105	108	120
Film after annealing at 550 °C in Argon	72	65	68	75	-	70
The Film after annealing at 550 °C in Ar + 4% H_2	348	320	360	332	-	340
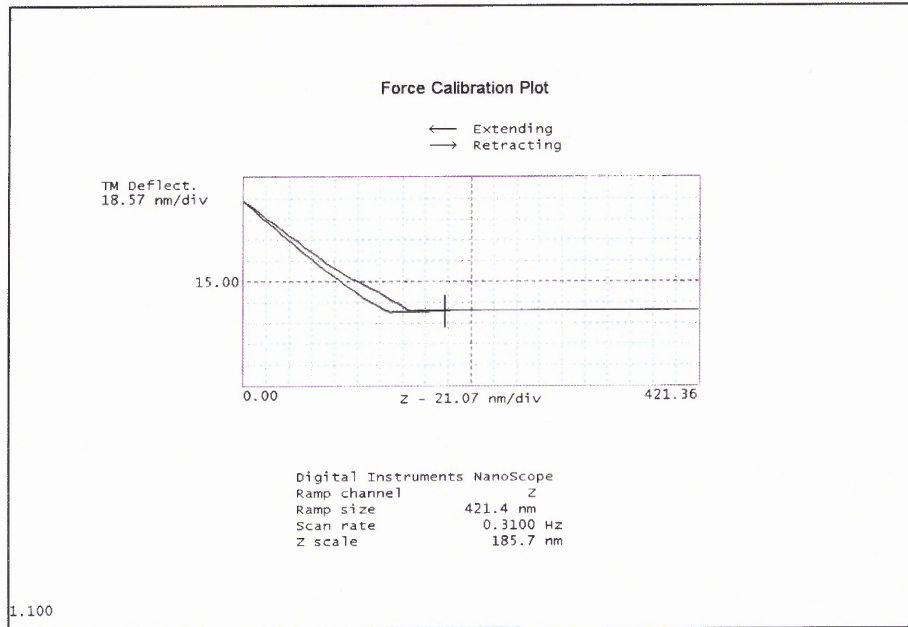
(a)
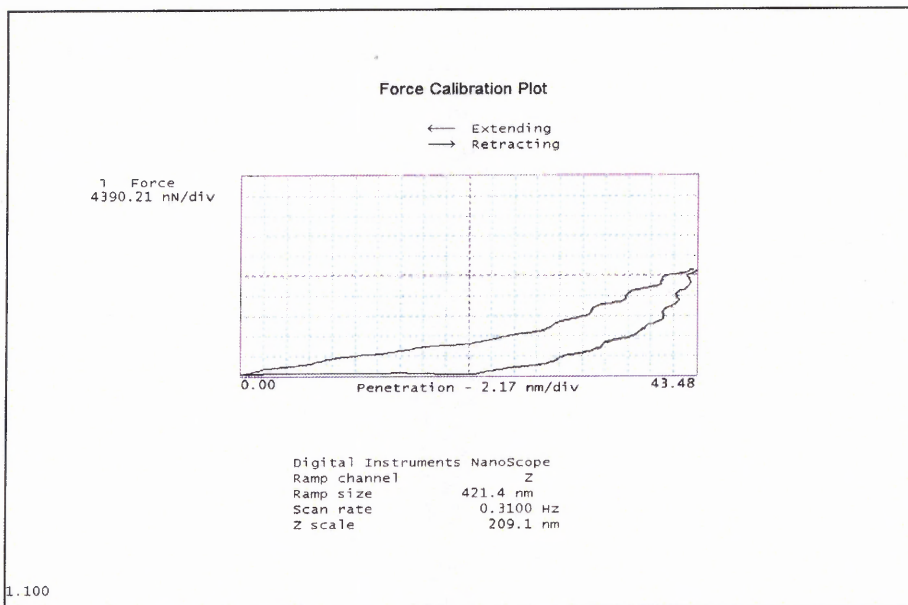
(b)

Fig.4.9 Nanoindentation results of as-deposited silicon film (a) force-movement curve; (b) loading-unloading curve.

Force Calibration Plot

⟵ Extending
⟶ Retracting

TM Deflect.
11.18 nm/div

7.55

Z - 19.25 nm/div

0.00   385.02

Digital Instruments NanoScope
Ramp channel   Z
Ramp size   385.0 nm
Scan rate   0.2906 Hz
Z scale   111.8 nm

2.001

(a)

Force Calibration Plot

⟵ Extending
⟶ Retracting

1   Force
2643.08 nN/div

0.00   Penetration - 2.00 nm/div   39.95

Digital Instruments NanoScope
Ramp channel   Z
Ramp size   385.0 nm
Scan rate   0.2906 Hz
Z scale   125.9 nm

2.100

(b)

Fig.4.10 Nanoindentation results of silicon film annealed in argon 550 ^{o}C for 30 minutes (a) force-movement curve; (b) loading-unloading curve.
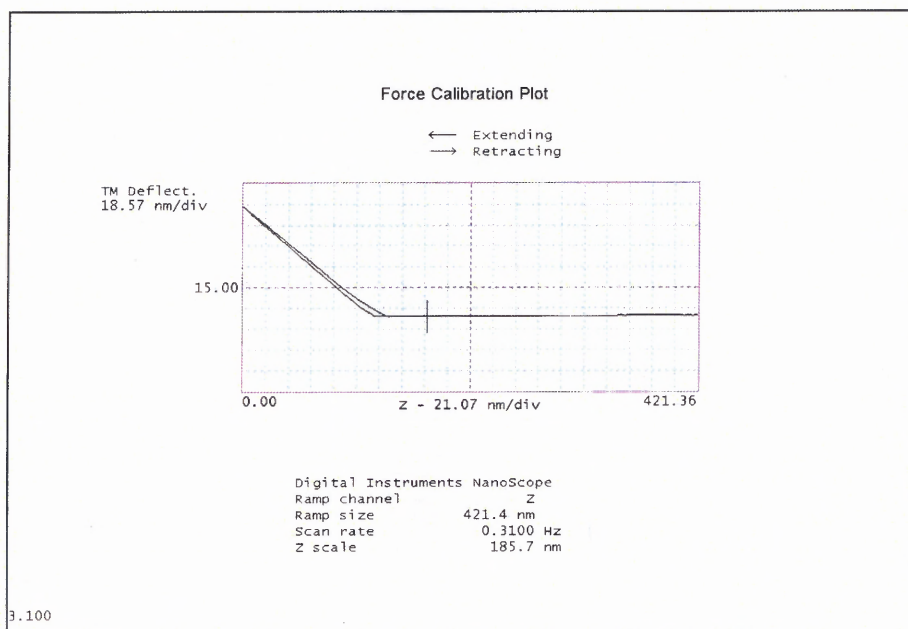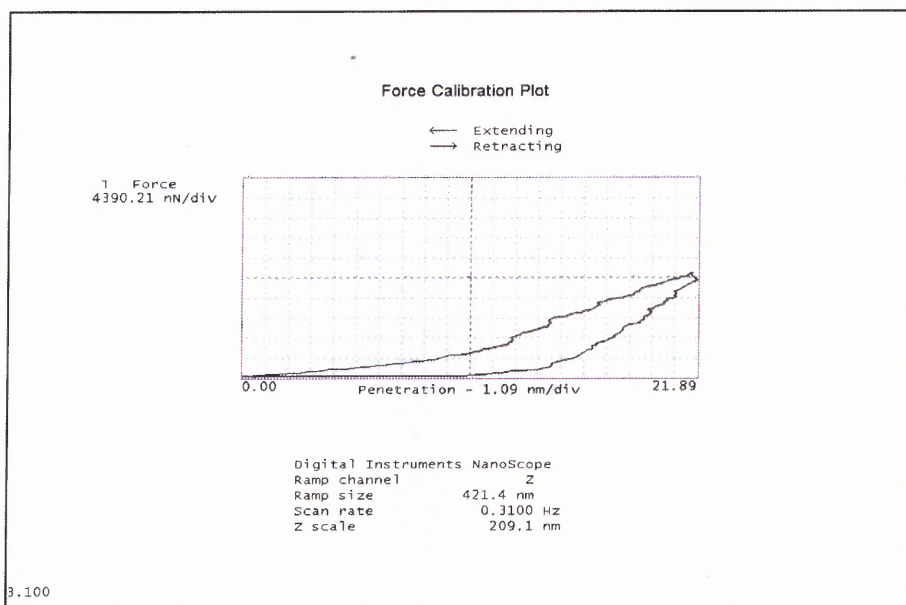
(a)

(b)

Fig.4.11 Nanoindentation results of silicon film annealed in argon + 4% hydrogen at 550 $^{\circ}$C for 30 minutes (a) force-movement curve; (b) loading-unloading curve.

4.2.4 Electrical Characterization

The electrical characterization was done by measuring the voltage-current curve of the samples. The V − I curves were obtained by both two probe measurement and scanning tunneling microscope. The method of STM has been introduced in chapter 3. In two probe measurement, a voltage is applied across the film and the resulted current was measured, the contact area between the electrode and the sample is around $1mm^2$. In the STM measurement, a voltage is applied between the sample and the STM tip and tunneling current is measured. Figure 4.12 to 4.14 are the measurement results on samples of as-deposited silicon film, and the films after annealing at 550 ^{o}C in argon and argon with hydrogen. The V − I curves reveal a characteristic of ohm contact between the silicon film and the underlying aluminum film.
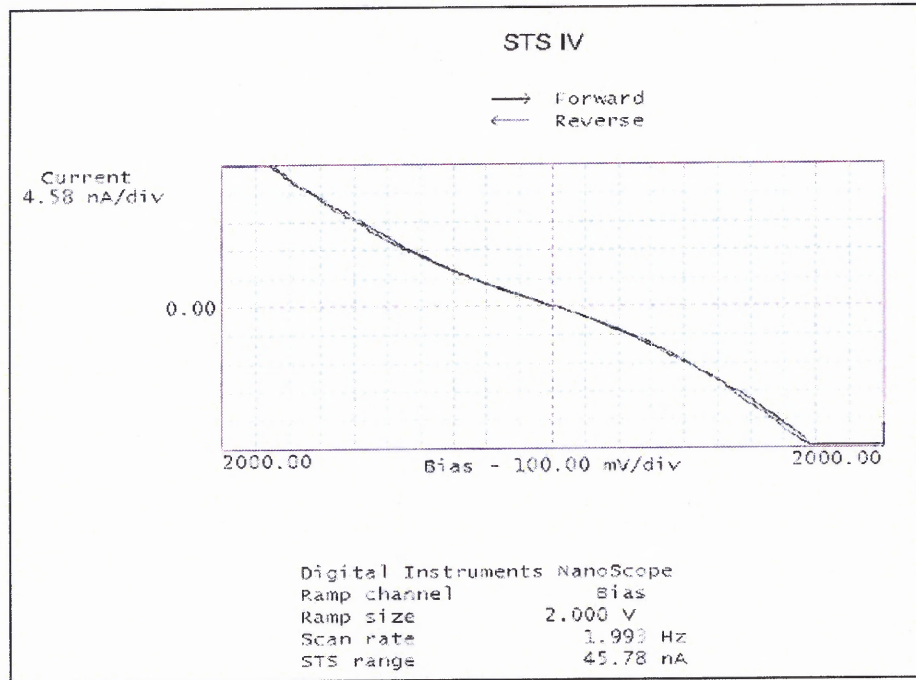
(a)
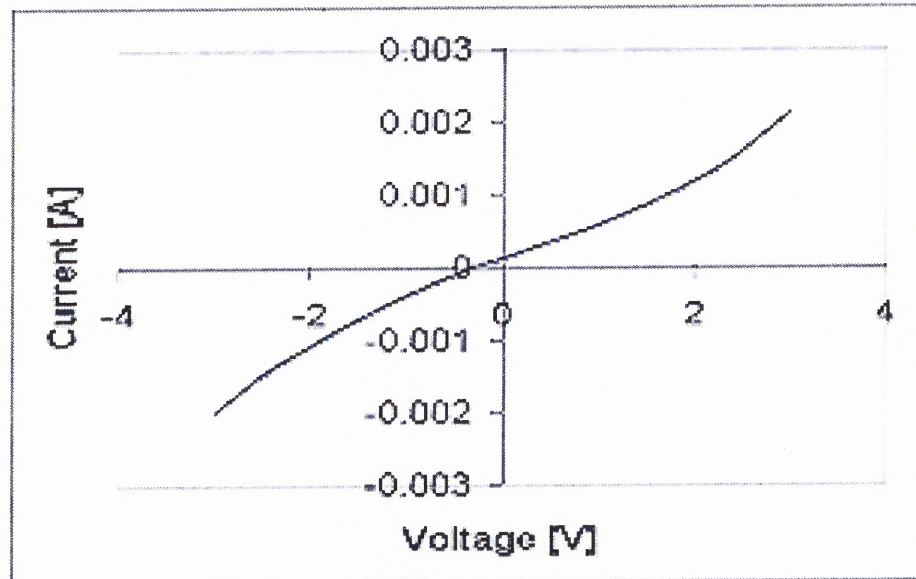
(b)

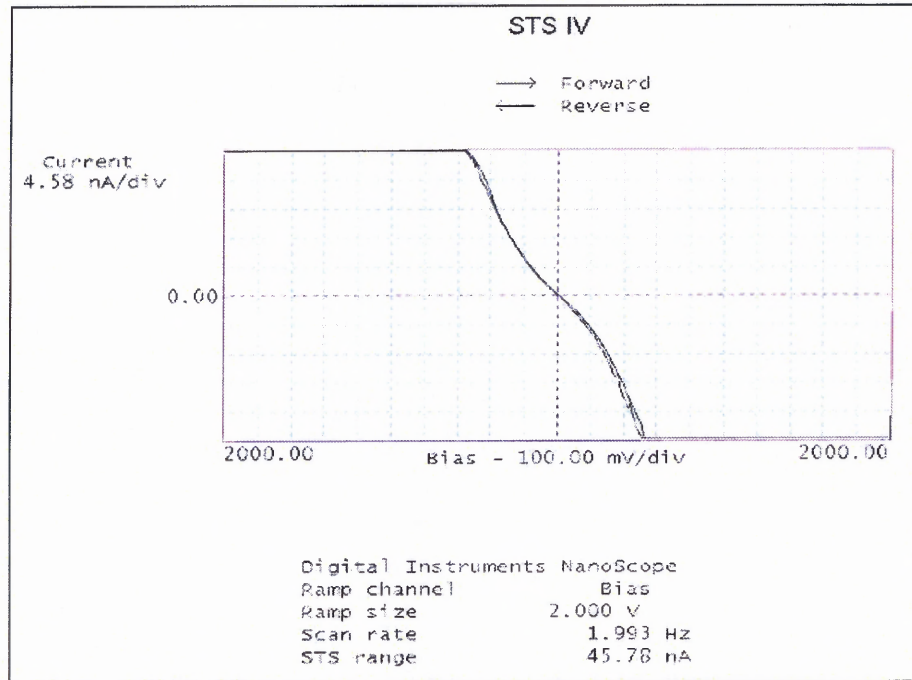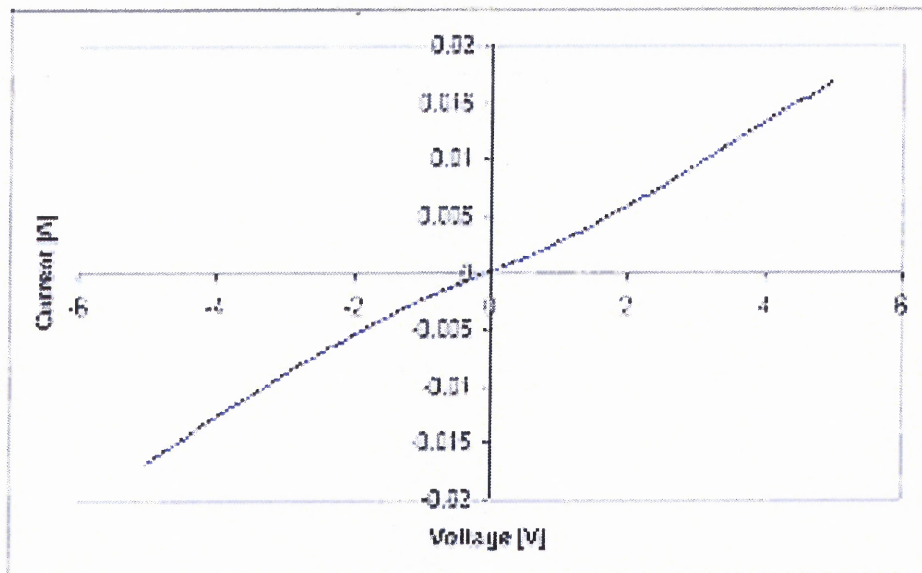**Fig.4.12** Voltage – current curves of as-deposited silicon film (a) by STM; (b) direct measurement
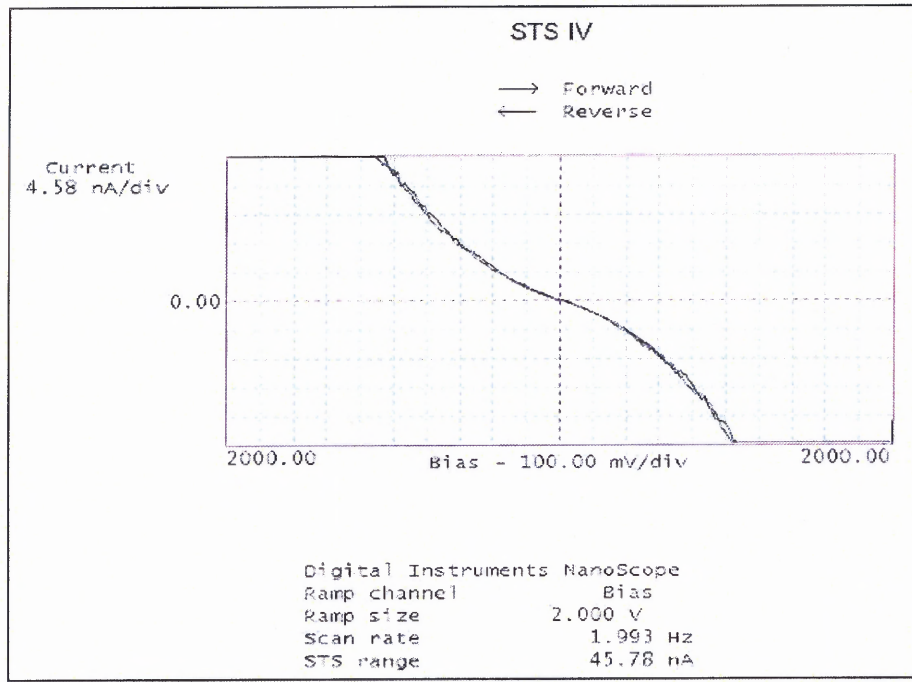
(a)

(b)

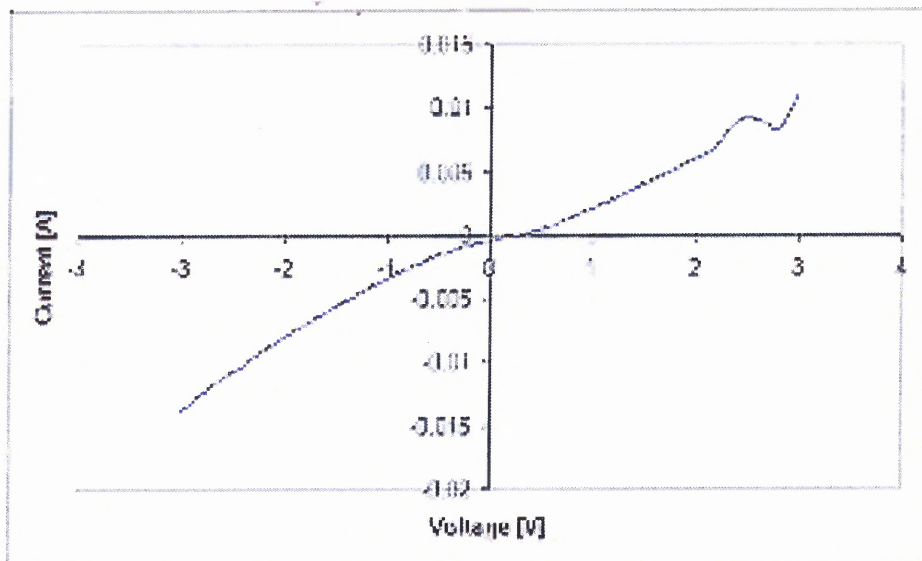**Fig.4.13** Voltage – current curves of silicon film annealed in argon at 550 °C for 30 minutes (a) by STM; (b) direct measurement

(a)

(b)

Fig.4.14 Voltage – current curves of silicon film annealed in argon at 550 ^{o}C for 30 minutes (a) by STM; (b) direct measurement

4.3 Discussion

From the experimental results on the structure and morphology study of the laser ablated silicon films, we found that the as deposited films were composed of crystalline droplets scattered among smooth featureless material which may consist of amorphous matrix. The crystalline nature of the droplets was confirmed by the Raman measurements. We observed Raman shifts for the laser ablated silicon droplets that are different from the silicon target. The position of the Raman shift suggests crystal symmetry of hexagonal silicon. This interesting observation leads us to think what the mechanism of the hexagonal silicon formation is during the laser ablation.

We know that silicon undergoes a series of phase transformation under high pressure or contact loading conditions, as shown in Fig.4.15 [1]. There are two known ways for the cubic diamond silicon to transform to hexagonal silicon, i.e. directly from cubic silicon with increasing pressure or by annealing of amorphous silicon at elevated temperature. Firstly, we discuss the morphology of the droplets. The droplets have a splash pattern, indicating that they were formed from the incident particulates in molten state. The silicon target after the laser ablation, as shown in Fig.4.16, displays a morphology that consists of craters and cavities. It also suggests that the target has been melted by the laser beam.

One mechanism that has been proposed for this particulate ejection and crater formation is explosive boiling or so-called phase explosion [11-14]. The concept of explosive boiling can be illustrated as in Fig.4.17 [12]. First, the incident laser creates a large population of highly excited electrons near the target surface. The excited electrons

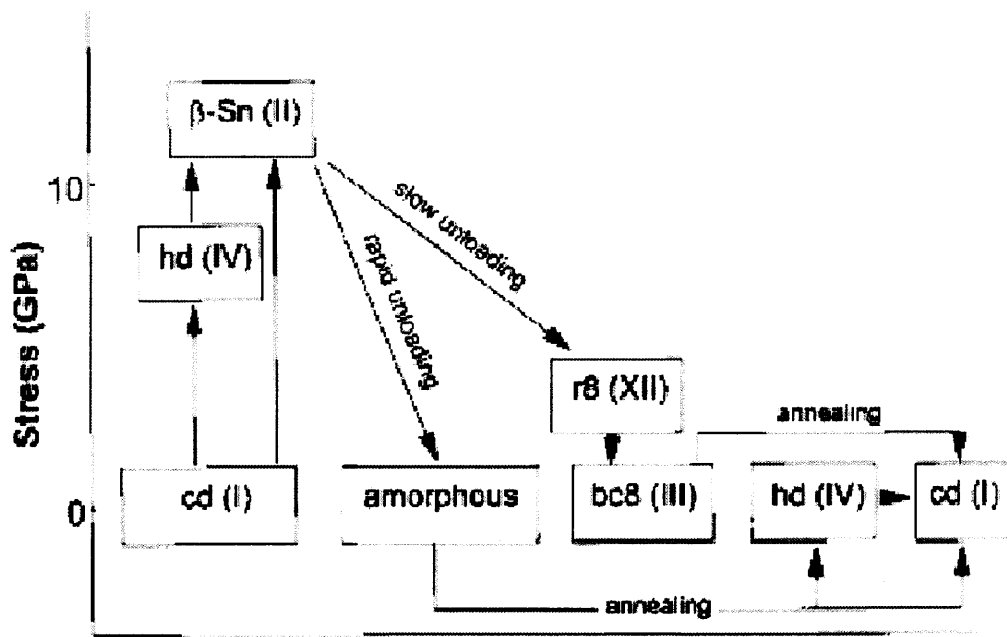**Fig.4.15** Diagram shows the phase transformation of silicon [1].
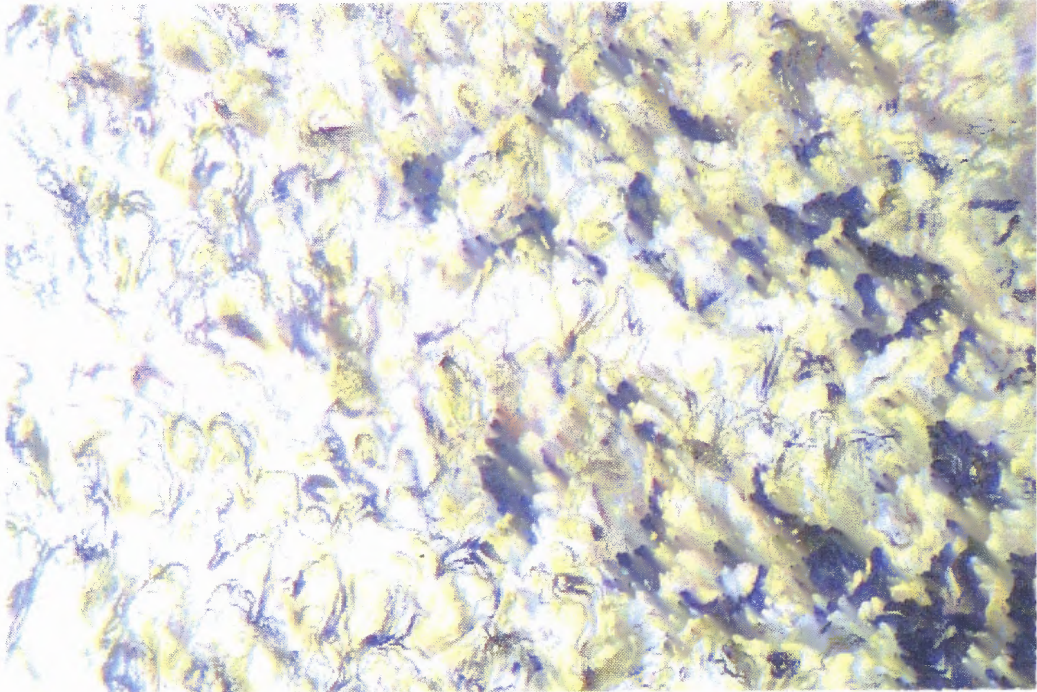
Fig.4.16 Optical micrograph of the silicon target after 10 minutes of laser ablation

laser pulse

superheated liquid

thermal penetration
layer (high T area)

during laser pulse

thermal diffusion

after laser pulse
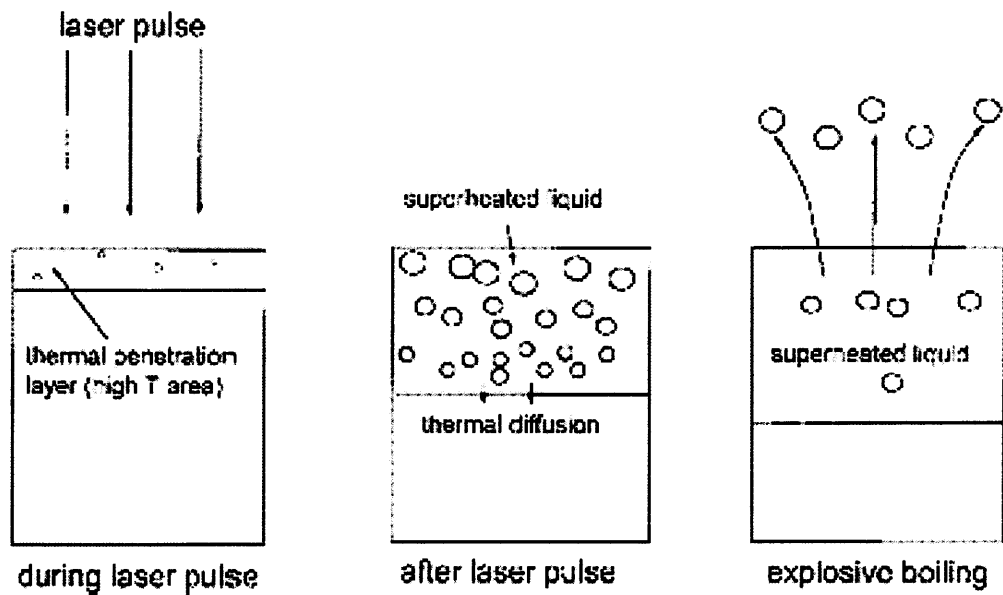
superheated liquid

explosive boiling

Fig.4.17 Schematic of the explosive boiling process during laser ablation [12].

transfer energy to photons in the electron-phonon relaxation. Heat is conducted into the target through lattice vibration. The heat melts the target and locally brings the temperature above its normal boiling point. Thus the material can reach to a metastable state of super heated fluid. It was suggested that the superheated silicon makes a transition from liquid metal to liquid dielectric, which facilitates further penetration of the incident laser light into the liquid-solid interface of the target and the liquid layer becomes thicker [11]. Next, vapor formed by density fluctuations near the critical state homogeneously nucleates as bubbles. Once these bubbles reach a critical size, they expand rapidly and initiate explosive boiling and mass ejection in the form of particulates [14].

It is not clear when the phase transformation of the cubic silicon to the hexagonal silicon occurs. The substrate was at room temperature at the start of the deposition and is believed to be close to room temperature during the whole deposition process. This seems to exclude the possibility of the re-crystallization of the amorphous silicon on the substrate. This assumption is further confirmed by the amorphous regions between the droplets. The amorphous material may be formed by rapid cooling of liquid or vapor on the substrate surface. To form crystal, there must be a critical size of the emitted mass. For the mass ejection that above this critical size, is likely generated by the explosive boiling process. The large size of the ejected molten mass enables the particulate to nucleate within itself. So the nucleation temperature may be within the droplet itself instead of the substrate temperature. A recent study on the femtosecond laser ablation of single crystal silicon has observed phase transition on the laser irradiated spot on the

target, which confirms the possibility of phase transition through melting, amorphisation and rapid local re-crystallization.

For the annealing experiments results, the conversion of hexagonal silicon back to the cubic diamond structure agrees with the observation by other researchers [1, 2]. The presence of hydrogen in the annealing atmosphere helps to stabilize the hexagonal structure. Hydrogen is known to saturate silicon bonds and may help prevent their rearrangement needed for the phase transformation. The mechanism is not clear at this time and more experiments need to be carried out to investigate the effect of the hydrogen.

Preliminary electrical and mechanical characterizations have been done on the deposited films. There have been certain difficulties in those experiments due to the size and the unevenness of the droplet surface. There have been large variations in the Young's modulus results obtained from the nanoindentation test. The Young's modulus of the as-deposited hexagonal silicon is larger than that of the cubic silicon obtained by annealing of the films in argon. But annealing of the hexagonal crystals in argon with hydrogen increases the young's modulus above the value measured on the as-deposited material.

CHAPTER 5

CONCLUSIONS

In this research, silicon films have been deposited by nanosecond UV laser ablation and characterized with a variety of experimental methods. The following conclusions can be drawn from the results of these experiments.

1. Hexagonal silicon crystals have been obtained by nanosecond pulsed laser ablation method on both quartz and aluminum coated quartz substrates. The topographical studies revealed that the deposited silicon film consists of crystalline droplets with size of 5 to 25 um scattered on top of a featureless, amorphous matrix.

2. The Raman spectra of the as-deposited crystalline droplets show a Raman shift that agrees with a hexagonal symmetry. It conforms that hexagonal polymorphs of silicon were formed.

3. The hexagonal crystal structure of the droplets transforms to the cubic-diamond structure during annealing at 550°C for 30 minutes in the inert atmosphere of argon. This phase transformation does not occur if hydrogen at the concentration of 4 percent is added to argon. It is confirmed by Raman measurements. .

4. The Young's modulus for the as-deposited hexagonal silicon measured by the nanoindentation method is larger than that of the cubic silicon obtained by annealing in argon. The young's modulus of hexagonal silicon crystals increases after annealing in argon with hydrogen.

5. The I-V curves were obtained by both direct measurement and scanning tunneling microscope. The I-V curves reveal a characteristic of ohmic contact between the silicon film and the underlying aluminum film. It also shows that the resistance decreases after annealing.

6. Based on the morphology of the deposited film and the morphology of the silicon target subjected to laser ablation, we postulate that a process of explosive boiling is as the mechanism of the formation of the hexagonal crystalline droplets.

REFERENCES

1. A. Kailer, Y. G. Gogotsi, and K. G. Nickel, "Phase transition of silicon caused by contact loading," J. Appl. Phys., 81 (7), Aril 1997, pp. 3057 – 3063.

2. V. Domnich, and Y. Gogotsi, "Phase transformations in silicon under contact loading," Rev. Adv. Mater. Sci., 2, 2002, pp. 1-36.

3. Y. Zhang, Z. Iqbal, S. Vijayalakshmi, and H. Grebel, "Stable hexagonal-wurtzite silicon phase by laser ablation," Appl. Phys. Lett., 75 (18), Nov. 1999, pp. 2758 – 2760.

4. S. Vijayalakshmi, A. Lan, Z. Iqbal, and H. Grebel, "Nonlinear optical properties of laser ablated silicon Nanostructures," J. Appl. Phys., 92 (5), Sep. 2002, pp. 2490 – 2494.

5. J. C. Miller (Ed.), Laser Ablation: Principle and Applications, Springer-Verlag, 1994.

6. L. Reimer, Scanning Electron Microscopy: Physics of Image Formation and Microanalysis, Springer, 1998.

7. M. Ohring, Materials Science of Thin Films: Deposition and Structure, Academic Press, 2002.

8. http://www.veeco.com.

9. C. R. Blanchard, "Atomic force microscope," The Chemical Educator, 1 (5), Sringer-Verlag, 1996.

10. P. West, and N. Starostina, "A guide to AFM image artifacts," Pacific Nanotechnology, Inc., Santa Clara, CA.

11. J. H. Yoo, S. H. Jeong, R. Greif, and R. E. Russo, "Explosive change in crater properties during high power nanosecond laser ablation of silicon," J. Appl. Phys., 88 (3), August 2000, pp. 1638 – 1649.

12. Q. Lu, S. S. Mao, X. Mao, and R. E. Russo, "Delayed phase explosion during high-power nanosecond laser ablation of silicon," Appl. Phys. Lett., 80 (17), April 2002, pp. 3072 – 3074.

13. H. L. Spindler, R. M. Gilgenbach, and J. S. Lash, "Effects of alser-ablation target damage on particulate production investigated by laser scattering with deposited thin film and target analysis," Appl. Phys. Lett., 68 (23), june 1996, pp.3245 – 3247.

14. V. Craciun, N. Bassim, R. K. Singh, D. Craciun, J. Hermann, C. Boulmer-Leborgne, "Laser-induced explosive boiling during nanosecond laser ablation of silicon," Appl. Surf. Sci., 186, 2002, pp. 288 – 292.